Technische Universität Berlin

Institut für
Werkstoffwissenschaften
und -technologien

- Metallische Werkstoffe -

Haroldo Pinto

Effect of Temperature and Environment on the Deformation Mechanisms of Austenitic Steels during Cryogenic Wear

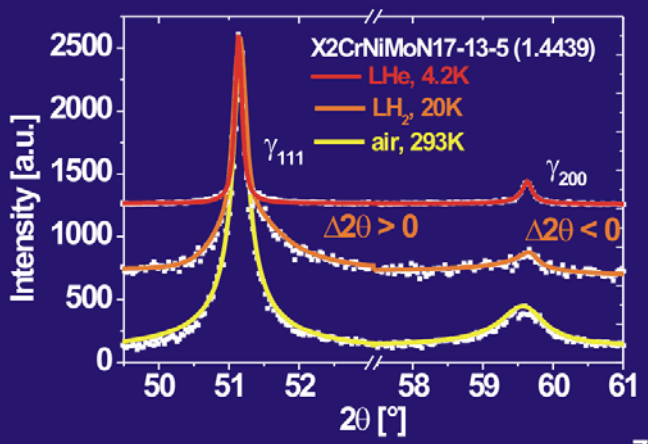

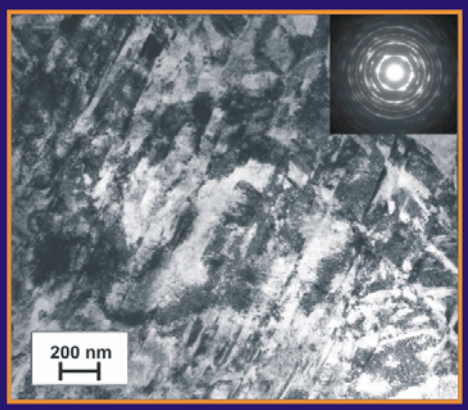

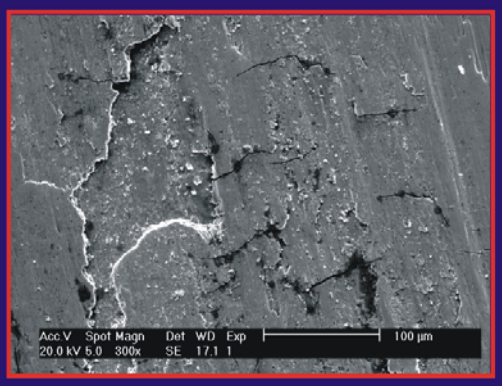

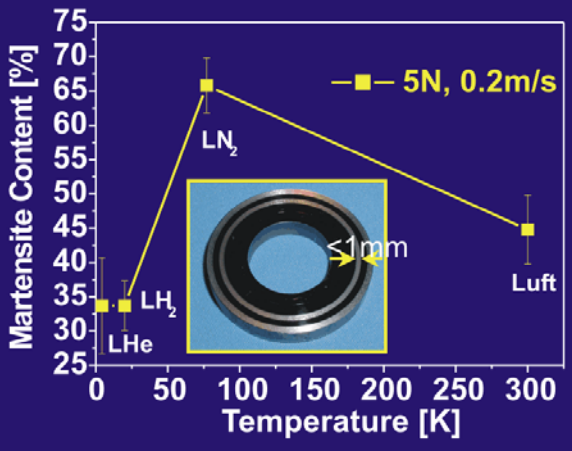

Effect of Temperature and Environment on the Deformation Mechanisms of Austenitic Steels during Cryogenic Wear

Effect of Temperature and Environment on the Deformation Mechanisms of Austenitic Steels during Cryogenic Wear

von
Diplom-Ingenieur
Haroldo Cavalcanti Pinto
aus Belo Horizonte, Brasilien

Von der Fakultät III
- Fakultät für Prozesswissenschaften -
der Technische Universität Berlin
zur Erlangung des akademischen Grades

Doktor der Ingenieurwissenschaften
- Dr.-Ing. -

genehmigte Dissertation

Promotionsausschuss:

Vorsitzender: Prof. Dr. M. H. Wagner
Berichter: Prof. Dr. rer. nat. W. Reimers
Berichter: Prof. Dr.-Ing. A. Pyzalla
Berichter: Prof. Dr.-Ing. A. Fischer

Tag der wissenschaftlichen Aussprache: 09. Juni 2005

Berlin 2005
D83

ABSTRACT

Haroldo Cavalcanti Pinto

Effect of Temperature and Environment on the Deformation Mechanisms of Austenitic Steels during Cryogenic Wear

The low temperature technology comprises developments in the space technology and applications of superconductivity. Cryogenic temperatures are encountered e.g. in superconducting magnets and magnetic resonance tomographs, where liquid helium (LHe) is employed as cooling agent, and in the aerospace technology, where liquid hydrogen (LH_2) became the standard propellant. Hydrogen represents an important alternative to fossil fuels. The liquefied form, at cryogenic temperatures of about 20K, is particularly attractive due to the possibility of stocking a large quantity of hydrogen within a small volume. In moving machine parts cryogenic temperatures and the presence of hydrogen strongly affect the deformation mechanisms and subsequently component failure.

Austenitic stainless steels are materials commonly used in cryotechnology. At extremely low temperatures these steels still exhibit good mechanical properties along with sufficient ductility. However, high mechanical loads combined with low temperatures may induce martensitic transfomation. The formation of martensite within the worn surface enhances strength but also causes embrittlement. This could influence the degradation process of cryogenic machine components and disturbs the superconductive effect due to its ferromagnetism.

The aim of the present work was the investigation of the influence of temperature, environment and loading conditions on the martensitic transformation and the microstructural deterioration of austenitic stainless steels during cryogenic wear. X-ray diffraction and microscopy studies were carried out on samples worn at room temperature in air with different humidities, at 77 K in LN_2, at 20 K in LH_2 and at 4.2 K in LHe. Results show that martensitic transformation in austenitic steels can be supressed by increased Ni-contents or its replacement by Mn. It can be shown that strain induced α-martensite does not cause a loss of wear resistance at cryogenic temperatures. A decrease of temperature causes changes in the deformation mechanisms and results in embrittlement in liquid hydrogen. The amount of hydrogen induced surface cracks depends on the alloy composition and is not necessarily correlated to the wear resistance of the austenitic steels.

ABSTRACT

Haroldo Cavalcanti Pinto

Effect of Temperature and Environment on the Deformation Mechanisms of Austenitic Steels during Cryogenic Wear

Die Tieftemperatur-Technologie findet Anwendung in der Raumfahrttechnik und in der Supraleitung. Kryogene Temperaturen treten z.B. in supraleitenden Magneten und Kernspintomographen auf, wo flüssiges Helium (LHe) als Kühlmittel eingesetzt wird, und in der Raketentechnik, wo sich flüssiger Wasserstoff (LH_2) als Standardtreibstoff bewährte. Wasserstoff stellt eine wichtige Alternative zu fossilen Brennstoffen dar. Bei kryogenen Temperaturen von etwa 20 K ermöglicht die flüssige Form, große Wasserstoffmengen in einem kleinen Volumen speichern zu können. In beweglichen Maschinenkomponenten beeinflussen sowohl tiefe Temperaturen als auch die Anwesenheit von Wasserstoff die Verformungsmechanismen und dementsprechend das Versagen von Bauteilen.

Austenitische rostfreie Stähle werden in der Kryotechnik als Standardwerkstoffe eingesetzt. In tiefkalten Medien verfügen diese Stähle noch über eine gute mechanische Festigkeit mit ausreichender Duktilität. Hohe mechanische Belastungen bei extrem tiefen Temperaturen können jedoch zur martensitischen Umwandlung führen. Die Martensitbildung innerhalb der verschlissenen Oberfläche erhöht die Festigkeit, führt aber zur Versprödung. Dies kann den Schädigungsmechanismus von in tiefkalten Medien eingesetzten Bauteilen beeinflussen und stört den Supraleitungseffekt infolge seines ferromagnetischen Verhaltens.

Ziel dieser Arbeit war die Untersuchung des Einflusses von Temperatur, Umgebung und Belastung auf die martensitische Umwandlung und die Werkstoffschädigung von austenitischen rostfreien Stähle bei Kryoverschleiß. Untersuchungen mittels Röntgendiffraktion und Mikroskopie wurden an Proben, die bei Raumtemperatur und verschiedenen Luftfeuchten, bei 77 K im flüssigen Stickstoff, bei 20 K im flüssigen Wasserstoff und 4.2 K im flüssigen Helium verschlissen wurden, durchgeführt. Die Ergebnisse zeigen, dass sich die martensitische Umwandlung in austenitischen Stähle durch erhöhte Ni- und Mn-Gehalte unterdrücken lässt. Sinkende Temperaturen verändern die Verformungsmechanismen und führen zur Versprödung in LH_2. Die wasserstoffinduzierte Rissbildung hängt von der Legierungszusammensetzung ab und beeinflusst den Verschleißwiderstand der austenitischen Stähle nicht.

ACKNOWLEDGEMENTS

The present work was carried out during my three and half years activities as a scientific co-worker in the Working Group for Metallic Materials in the Institute for Materials Science and Technology of the Technical University Berlin (TU Berlin) and in the Working Group for Joining in the Institute for Materials Science and Material Technology of the Vienna University of Technology (TU Wien).

First of all I would like to express my thanks to Prof. Dr.-Ing. Anke Pyzalla not only for refereeing but also for fruitful discussions and suggestions and to Prof. Dr. rer. nat. W. Reimers for refereeing the thesis and his interest in this work. Prof. Dr.-Ing. A. Fischer is also greatly acknowledged for refereeing and valuable discussions.

I would like to thank also Prof. Dr.-Ing. M. H. Wagner for assuming the chairmanship of the thesis committee.

I greatly acknowledge the staff of the group ,,Cryo-, Hydrogen- and Vacuumtribology'' in the Federal Institute for Materials Research and Testing (BAM) in Berlin, specially Dr. W. Hübner and K. Aßmus, for the performance of all wear tests. Their good cooperation and fruitful discussions during the three years project were also indispensable. Dr. T. Gradt is thanked for his numerous helps on providing me all wear data during the last phase of my work.

Prof. Dr.tech. H.-P. Degischer and Prof. Dr.tech. S. Seidler at the TU Wien are acknowledged for promoting a good atmosphere and working conditions at our institute in Vienna.

Dr. T. Link at the TU Berlin and M. Klaus now at BESSY Berlin are specially thanked for their assistance during the TEM investigations.

The Hamburger Synchrotronstrahlungslabor (HASYLAB) in Hamburg is also kindly acknowledged for the numerous allocation of beamtime needed for my research. Many thanks go to Dr. T. Wroblewski and Dr. B. Hasse for helpful support during the diffraction experiments at the beamline G3.

The Deutsche Forschungsgemeinschaft (DFG) is acknowledged for the financial support (Project Py9/4-1).

I would like to express my thanks also to my dear colleagues, B. Reetz, Dr. S. Dieter and E. Wild at the TU Berlin and K. Zimnik, P. Silva, R. Coelho, M. Moscicki, L. Ito, F. Sket, C. Juricic, R. Alavi Zaree, M. Crovace, A. Neta and L. Agudo at the TU Wien for the good cooperation and indispensable ,,cultural events'' over the last three and half years. My former colleagues E. Lima, M. Stempniewicz and I. Denks are in this sense also kindly acknowledged.

I am also grateful to M. Hill and M. Schaube at the TU Berlin and to H. Knoblich, J. Knoblich and S. Zellhofer at the TU Wien for their sincere help in the sample preparation. Many thanks go also to S. Fabian at the TU Berlin and H. Kaminski at the TU Wien for their permanent technical support in the X-ray laboratories. C. Zaruba, TU Wien, is acknowledged for his continuous help in solving my computer troubles and during the SEM sessions in Vienna. H. Malks, TU Berlin, was very helpful during my SEM investigations in Berlin. S. Stuke, W. Mrkonjic and V. Strawson took part in my work as student co-workers and are here also acknowledged.

My last but not least thanks go to my parents, Hélio S. Pinto and Eduiges A. C. Pinto, and to my brother, Renato C. Pinto, for their steady encouragement over all these years.

Vienna, April 2005 Haroldo Cavalcanti Pinto

TABLE OF CONTENTS

1 Introduction

The low temperature technology comprises developments in space technology and applications of superconductivity. Cryogenic temperatures are encountered e.g. in superconducting magnets and magnetic resonance tomographs, where liquid helium (LHe) is employed as cooling agent, and in the aerospace technology, where liquid hydrogen (LH_2) became the standard propellant. To a minor extent cryogenic engineering appears in cryogenic treatments of ferrous and non-ferrous materials and medical applications. Furthermore, many efforts are being done to employ liquid hydrogen as an environmental friendly energy supply. Since hydrogen represents an important alternative to fossil fuels, the production of hydrogen on a large scale along with its compatibility to the current technology of internal combustion engines are of great technological concern in the automotive sector. Hydrogen storage is possible in tanks as a gas, at room temperature (RT) at about 20MPa pressure, and in a liquefied form, at cryogenic temperatures of about 20K. The latter form is particularly attractive due to the possibility of stocking a large quantity of hydrogen within a small volume.

Due to the impracticable use of lubricants at extremely low temperatures, cryogenic tribosystems are critical with respect to wear and frictional heat generation. Wear processes are often connected with an unexpected failure of valves and bearings. Undetected leaks, which can develop during service, can cause uncontrolled escape of gas. Hence ignitable gas mixtures may occur and in case of hydrogen, oxygen can produce violent fire. On the other hand, frictional heating, produced by the rapid slip of conductors against each other in superconducting magnets, is frequently capable of raising the local conductor temperature to above its superconducting transition temperature.

In addition, the tribological behavior of materials used in the cryo-technology must be evaluated within a wide temperature range. Machine components are usually exposed to thermal cycles and are, therefore, stressed at room temperature (RT) as well. Nevertheless the material properties at cryogenic temperatures must be preserved. Thermal cycles acting additionally to tribological loading are encountered e.g. in components of satellites and space shuttles, which are tested on the ground at RT but should resist service temperatures down to 1K [LIN01], as well as in

components of aircrafts using LH_2 as propellant, where depending on the fuelling state considerable temperature fluctuations can be observed [POH96].

Therefore, materials for cryo-engineering have to be resistant to extreme conditions of simultaneous influence of low temperatures, plastic deformation at the surface and in special environments, such as reactive hydrogen or oxygen environments. Due to the combination of high mechanical strength with sufficient ductility and chemical resistance, austenitic stainless steels belong to one of the most important groups of materials for cryogenic applications. In applications of superconductivity these alloys are also commonly used due to their non-magnetizing properties. However, austenitic steels may undergo a strain-induced martensitic transformation [SCH75I], which is especially favored by low temperatures. The formation of martensite within the worn surface enhances strength but also causes embrittlement. This may influence the degradation process of cryogenic machine components and consequently their lifetime. Furthermore martensite is ferromagnetic and thus its formation needs to be prevented in applications of superconductivity as well.

The aim of the present work is the study of the influence of chemical composition, temperature, environment and tribological stress conditions on the stability of the austenitic microstructure, the deterioration process and the wear behavior during friction in cryogenic media of five different austenitic steels, which are currently in use. They provide a continuous variation of the stacking fault energy (SFE) as well as of the austenite stability mainly due to their different Ni-, Mn- and N-contents. The investigations attempt to correlate the SFE and its dependence on temperature and environment with the microstructural modifications and the wear performance.

2 State of the Art

2.1 Materials for cryo-engineering and hydrogen technology

Some years ago, the handling of hydrogen was restricted essentially to the chemical industry without causing major problems. Recently the hydrogen technology underwent a rapid development and the field of applications in this area has considerably increased. Hydrogen is regarded as an efficient and environmental friendly energy resource for the near future [DWV00]. The International Hydrogen Energy Forum HYFORUM 2000 in Munich showed, that liquid hydrogen (LH_2) plays an important role [HYF00], especially as storage medium [SPI98]. BMW started already the serial production of cars with hydrogen combustion machines and these cars became a part of an EXPO 2000 project in Munich. At the same time the Deutsche Aerospace Airbus (DASA) is developing the prototype of an aircraft with hydrogen engines [BER00].

These new technologies involve challenging requirements concerning the mechanical properties of materials used for hydrogen storage. In hydrogen technology attention has to be paid to safety aspects. The failure of machine components may lead to an uncontrolled escape of hydrogen and consequently to the formation of an explosive atmosphere.

There are only few labs, which can carry out tests in liquid hydrogen. In Europe only the Federal Institute for Materials Research and Testing (BAM) in Germany and the Institute of Low Temperature Physics and Technology of the Ukrainian Academy of Science are capable of performing tribological tests in cryogenic environments containing hydrogen [OST01].

Most important works on material behavior in liquid hydrogen have been performed for applications in space (rocket) technology. Only materials, which are already established in their respective applications, are being investigated regarding their properties in hydrogen. The behavior of FeCrNi-alloys in hydrogen is not conclusively investigated either. Present studies deal particularly with the different deformation behavior of steels in liquid helium and hydrogen [DEI01]. However, new materials for cryogenic applications, such as light metal alloys and polymer composites, are being increasingly developed [FRI01].

2.2 Austenitic CrNi-Steels

CrNi steels contain besides iron and carbon, chromium and nickel in very distinct contents. Fig.1 shows the Maurer-Diagram, which gives an overview about the microstructure formation in CrNi-steels with 0.2% C after water quenching from 1050°C. Using slower cooling rates, the borderlines are shifted towards higher Ni-contents.

The outstanding mechanical and technological properties of the classic austenitic CrNi-steels as well as their good corrosion resistance, weldability and cold workability are responsible for the manifold applications of this steel grade. The fcc crystal lattice at RT is metastable and provided by sufficient contents of alloying elements, which stabilize the austenite, such as Ni. Under equilibrium conditions the microstructure of CrNi-steels consists of austenite, δ-ferrite and $(Cr,Fe)_{23}C_6$. Cr is in principle a ferrite stabilizer, but it hampers the transformation of an undercooled austenite into ferrite. Thus, the presence of Cr usually reduces the Ni-content necessary to obtain a metastable austenite at RT. For 18% Cr-content a minimum Ni-fraction of 8% is necessary to obtain an austenitic steel. Higher as well as lower Cr-contents require higher Ni-additions to keep an austenitic microstructure at RT. The stability of the austenite depends also on the other alloying elements, which can be classified according to their effect in the ‘’Cr-equivalent’’ and ‘’Ni-equivalent’’. The first one comprises, besides Cr, elements such as Si, Mo, V and Al, and the latter one contains, besides Ni, elements like Co, Mn, N and C. The effect of the chemical composition on the expected microstructure is displayed in the so-called Schaeffler-Diagram (Fig.2).

However, the metastable austenite may transform to strain-induced martensite during plastic deformation of the steel. Two forms of martensite exist in low carbon austenitic steels: hexagonal close packed (hcp) ε-martensite and body-centered cubic α’-martensite. During the early stages of deformation, shear bands consisting of stacking faults (SF) and ε-martensite form on the {111} planes of austenite. Partial dislocation movements on successive $\{111\}_\gamma$ lattice planes form twins and on alternate such planes ε-martensite [DIA98]. The α’-martensite nucleates at the intersection of shear bands. As the deformation level increases, the α’-martensite volume fraction grows at the expense of the ε-martensite.

The amount of ε- and α'-martensites is controlled essentially by two parameters: M_{d30}-temperature (at which after 30% plastic deformation martensite formation starts) and stacking fault energy (SFE). The M_{d30}-temperature is determined by the composition and the grain size of the steel. The SFE of the steel depends on the chemical composition and increases with increasing temperature. If the SFE is higher than 100 mJ/m^2, a direct γ→α' transformation is expected under load. This value is only very slightly influenced by the complicated shearing mechanism occurring during lattice change under external stresses or strains.

The tendency to form extended stacking faults (SF) or hexagonal ε-martensite increases as the SFE is lowered by adding of certain alloying elements, such as e.g. Cr + Ni, Cr + Mn or Mn + C. Then the indirect γ→ ε → α' or γ→ SF → α'-transformation occurs, where ε-martensite and stacking fault only gradually differ from each other. Due to the simple shearing mechanism of the γ/ε and γ/SF transformation, external stresses strongly favor the indirect transformation. Especially in crossing regions of ε-plates or SF, but also in their internal parts, shear processes are generated, which are pre-stages or nuclei of α'-crystals. If the SFE is lower than 20 mJ/m^2, complete strain induced martensite formation becomes possible, if this is in accordance with the thermodynamic stability relations [SCH75I].

Several empirical equations have been developed to calculate the values of M_d-temperature and SFE. Nohara et al. [NOH77] determined empirically the following equation to calculate the M_{d30}-temperature:

$$M_{d30}\,[°C] = 551 - 462(\%C + \%N) - 9.2\,\%Si - 8.1\,\%Mn - 13.7\,\%Cr - 29\,(\%Ni + \%Cu) - 18.5\,\%Mo - 68\,\%Nb - 1.42\,(GS - 8) \quad (1)$$

where GS is the ASTM grain size number. For calculating the SFE different approaches are used depending on the alloy composition. Rhodes and Thompson [RHO77] derived the following equation to evaluate the SFE of austenitic stainless steels:

$$SFE\,[mJ/m^2] = 1.2 + 1.4\,\%Ni + 0.6\,\%Cr + 17.7\,\%Mn - 44.7\,\%Si \quad (2)$$

2.3 Non-magnetic Steels

Austenitic steels are used in applications, where disturbing interactions with magnetic field lines should be avoided. One of the recent and important uses of austenitic

stainless steels is the cryogenic use as superconducting magnet structural material in the magnetic levitation transportation, large scale accelerators for particle collisions, fusion devices or storage tanks of liquefied natural gas, utilizing its non-magnetism or superior mechanical properties at cryogenic temperatures [KOH99].

In generating pulsed high magnetic fields, macrocomposite conductor materials play an important role. The main requirement for these conductor wires is a beneficial combination of high mechanical strength, high electrical conductivity and sufficient ductility. While a high ultimate tensile strength (UTS) of the steel is required to resist the Lorentz force, a high conductivity limits the Joule heating during a pulse and, hence, determines the attainable pulse time. A sufficient ductility is needed in order to deform the wire without cracks to a rectangular cross section by drawing as well as for winding it to a coil. Generally these principal requirements are in conflict with each other. Metals show either a high thermal or a high strength. Furthermore, the stronger materials are, the less ductile they are [FRE03].

In the past two decades copper/stainless steel (Cu/SS) macrocomposites, pioneered in Oxford [JON88], were introduced into pulsed high magnetic field coils and have since then developed further on. The great advantage of the Cu/SS macrocomposites in comparison to other conductor materials (commonly microcomposites) is the enhancement of the UTS as well as the conductivity when cooled down. The corresponding increase of UTS is usually about 30%. It has been proposed that high nitrogen stainless steels should be even better than the commonly used ones [JON97,MCH83] for these applications.

Regarding the non-magnetic properties, steels have to be free of δ-ferrite, even in segregated areas or after welding. In addition a transformation to bcc martensite during cooling or plastic deformation is not permitted. The latter is a consequence of bending and blanking a sheet or a consequence of moving machine components. Localized plastic deformation at notches during cryogenic service combines both pre-requisites for a martensitic transformation. In this case nitrogen is most helpful in stabilizing the austenite, thus avoiding δ-ferrite as well as martensite, which are both ferromagnetic. However, deformation at low temperatures entails martensitic

transformation and a higher alloy content is necessary to suppress the ferromagnetic phase.

The elements Ni, Mn, C and N stabilize the austenite but are supported by the ferrite forming elements Cr and Mo to a lesser extent, as can be deduced from the Schaeffler diagram (Fig.2). If very low service temperatures are necessary, the paramagnetic austenite may transform to antiferromagnetic or ferromagnetic austenite, depending mainly on the Ni content (Fig.3). The Néel temperature T_N, at which the transition from paramagnetic to antiferromagnetic austenite occurs, decreases as the Ni-content grows. Above 20 at% Ni the Curie transition temperature T_C from paramagnetic to ferromagnetic austenite increases with increasing Ni content.

The magnetic susceptibility κ per unit volume serves as a measure of the magnetization rate of non-magnetic steels. At room temperature (RT) the relationship between the magnetic polarization J and the magnetization field strength H is linear as follows:

$$J = \kappa H \qquad (3)$$

With decreasing temperature κ increases until T_N is reached. With further cooling κ decreases again.

Ni is the essential stabilizer of austenite, but beyond about 20 at% Ni an undesired ferromagnetic order of Fe and Ni appears. A lower Ni content seems to have a beneficial effect on the susceptibility, which is reduced via an antiferromagnetic transition. On the other hand a low Ni content favors the strain-induced martensite formation during cryogenic service. In this case nitrogen alloying offers a solution and enhances additionally the yield strength. However, the positive effect of N on mechanical strength and austenite stability is limited by insufficient toughness observed for high N contents. It has been shown [GAV99] that a ductile-to-brittle transition is encountered in some stable austenitic steels with N contents higher than 0.5 mass%. Nowadays the N content of non-magnetic steels for cryogenic applications ranges between 0.3 and 0.4 mass%, which is seen as a compromise between magnetic properties, mechanical strength and toughness.

3 Aims and Working Procedure

Aim:

The aim of the present work is an investigation of the microstructure stability and the deformation behavior of austenitic stainless steel grades with different chemical compositions and, consequently different stacking fault energies, during friction in cryogenic environments (liquid nitrogen, hydrogen and helium) and in air with different relative humidities.

The effect of liquid hydrogen (LH_2) on the deformation and wear behavior shall be evaluated. Furthermore the connection between SFE, deformation behavior and wear performance shall be revealed.

Working Procedure:

The materials chosen for the present investigations were the German steel grades: 1.4452, 1.4301, 1.4439, 1.4876 and 1.4591. Due to their different chemical composition they provide a continuous variation of the SFE.

Tribotests and Wear Behavior

The tribological experiments were carried out at low temperatures in inert media and in liquid hydrogen [GRA01,GRA01l]. In order to study the influence of the air humidity oscillating sliding tests at RT were conducted. For the study of the effect of temperature and environment air at RT, LN_2 at 77 K, LH_2 at 20 K and LHe at 4.2 K were employed in the sliding friction tests.

The normal force, the sliding speed and the sliding distance were varied. Scanning electron microscopy (SEM) was employed in order to study the wear mechanisms at the different temperatures and environments.

Strain-induced Martensitic Transformation

The volume fraction of martensite formed within the wear scars during friction was determined ex-situ using synchrotron X-ray diffraction. Synchrotron radiation played an important role in these investigations due to the much higher spatial resolution achievable if compared to conventional X-rays, the strongly parallel beam and high photon flux. These are requirements for analyzing very narrow scars (< 1mm width)

and materials strongly deformed with very broad reflection profiles. All steels chosen were analyzed concerning their austenite stability. The friction-induced martensite content was evaluated as a function of temperature, environment and loading conditions. Furthermore it had to be clarified under which conditions α'- or ε-martensite forms. Due to the inhomogeneity of the wear scars the phase analyses were carried out at different points in the scar.

Deformation Behavior

Cross sections of the worn steel discs were prepared for light and scanning electron microscopy. For the investigation of the modified surface layer and the deformation mechanisms transmission electron microscopy was used. The results of the microscopy studies were quantified and compared with the analysis of the synchrotron X-ray diffraction profiles. Using the obtained information a connection between temperature, environment, SFE and wear resistance on the one hand and the deformation behavior on the other hand should be provided. In LH_2 a distinct deformation behavior was expected. This effect of LH_2 should be correlated to the wear performance of the different steel grades investigated.

Internal Stress and Texture Analysis

Synchrotron X-ray diffraction should be used for the internal stress analysis due to similar reasons as in the phase analysis. The variation of the internal stress state with temperature and environment should be monitored and their influence on the microstructural deterioration in the near-surface zone had to be analyzed.

Texture analysis was performed using conventional X-ray radiation. Crystallographic preferential orientations are strongly connected to the active deformation mechanisms. Thus, the texture formation was studied as a function of temperature and environment and correlated to the deformation behavior.

4 Experimental Details

4.1 Materials

For the experiments two groups of steels were selected. The first group consists of four austenitic FeCrNi alloys, which have distinct Ni- and N-contents. The chemical composition of these four austenitic alloys and their SFE are given in tab.1. The SFE at RT were determined as described in [RHO77].

According to [BUT73] the susceptibility to strain-induced martensitic transformation increases with decreasing SFE. In fig. 4 the SFE of the FeCrNi-alloys is shown, and they are ordered with respect to their martensite volume fraction after 80% plastic deformation in tensile testing [BUT73]. Furthermore it has been shown for Cu-alloys and steels [FEL89,WER83,HSU80] that due to its influence on the active deformation mechanisms, the SFE plays an important role in the wear behavior. The other microstructural parameters, such as grain size and volume fraction of inclusions and δ-ferrite, which also affect the mechanical strength of austenitic steels, did not vary considerably for the different alloys investigated. Thus, a connection between SFE, deformation behavior, microstructural stability and wear performance is expected in the friction tests.

Steel 1.4301 (X5CrNi18-10) is a metastable austenite. Its SFE is very low; thus, strain-induced martensitic transformation is possible even at room temperature.

Steel 1.4439 (X2CrNiMoN17-13-5) is a so-called stable austenitic steel. Phase transformation is hampered due to its increased SFE. The steels 1.4876 (X10NiCrAlTi32-20) and 1.4591 (X1CrNiMoCuN33-32-1) contain very high contents of Ni, their SFE is rather high and the generation of martensite is unlikely.

The second steel group consists of the N-high alloyed CrMn steel 1.4452 (X13CrMnMoN18-14-3). CrMn steels represent a Ni-free alternative to the FeCrNi alloys. Its composition and SFE are also given in tab.1.

As counterbodies Al_2O_3 ceramic balls were used to avoid metal transfer to the steel samples.

4.2 Wear tests

4.2.1 Sliding friction

For the friction experiments, discs made of the austenitic steels with polished surfaces were installed in the ball-on-flat disc configurations of the test rigs. Friction was realized by sliding the counterbody against the rotating sample (see fig. 5).

The experiments were carried out at the Federal Institute for Materials Research and Testing (BAM), Division VIII.1, Working group ,,Cryo-, Hydrogen- and Vacuumtribology'', in Berlin, Germany, using the tribometers CT2 and CT3 which are suitable for experiments at low temperatures in inert media and in liquid hydrogen [GRA01]. Tribometer CT2 is installed in a bath cryostat, insulated by a vacuum superinsulation. The complete friction couple is immersed into the liquid cryogen. The test temperature corresponds to the boiling temperature of the cryogen applied (LN_2 = 77 K; LH_2 = 20.4 K; LHe = 4.2 K). Tribometer CT3 (fig. 6) is cooled by a continuous flow cryostat. The temperature can be controlled between 4.2 K (LHe cooling) and room temperature (RT). The friction unit is surrounded by a contact gas, at low temperatures usually He. Also, experiments in hydrogen gas atmosphere are possible. Because of the insufficient heat conductivity of the gas, under these conditions experiments were carried out at low friction power [THE02].

Since in LH_2 the tribological properties of the materials can be influenced by the low temperatures as well as by an hydrogen uptake, it was necessary to study also the friction and wear behavior in inert atmospheres in order to separate between temperature and medium effects. LHe (4.2 K) and LN_2 (77 K) were chosen as additional cryogenic environments. The CrNi steels were tested in inert environments at low temperatures and in LH_2. The steel 1.4452 was investigated only in air and in LH_2.

As parameters for the tribological tests a normal force F_N = 5 N, sliding velocity v = 0.2 m/s and sliding distance s = 1000 m were chosen. In the wear tests at RT in air the samples were subjected to various sliding distances for monitoring the strain-induced martensitic formation starting from the running-in period. In order to study the influence of the loading conditions the normal force was varied between F_N = 5 and 10 N and the sliding velocity between v = 0.06 and 0.2 m/s in the sliding tests performed in LH_2.

Scanning electron microscopy (SEM) at the BAM, Berlin, was used to measure the scar widths formed on the ball specimen, which were chosen as parameters for the wear resistance.

4.2.2 Fretting

Oscillating sliding tests at RT were conducted at the BAM, Division VIII.1, Working group ,,Oscillating Wear'', Berlin, in order to study the influence of air humidity (4, 50 and 100%) on the microstructural changes. During the experiments 100000 cycles were realized using F_N = 5 N, a stroke Δx = 800 μm and a frequency f = 20 Hz. Fig.7 shows the fretting-tribometer TKRD used for the investigations. For measuring the scar widths generated on the steel discs SEM was performed at the TU Wien.

4.3 Microstructural investigations

4.3.1 Light microscopy (LM)

Cross sections of the wear scars were prepared for LM studies using SiC-papers down to a grain size of 2400 and a diamond suspension down to 1μm. In order to reveal the microstructure an etching solution of 25ml HCl and 10ml of each glycerine, acetic and sulphuric acid was used as recommended in [AHN79]. At RT the samples were etched for 3 – 4 min and again in steps of 30 s until the microstructure was visible. LM micrographs were produced using the bright field modus.

4.3.2 Electron microscopy

The morphology of the wear scars and crack formation during friction in LH_2 were investigated using a scanning electron microscope (SEM). For the SEM investigations no special sample preparation was necessary, the wear scars were only cleaned in an ultrasound bath. Additionally, cross-sections of the wear scars were imaged using the SEM in order to investigate of the crack propagation from the top surface zone into the bulk material. Energy dispersive X-ray (EDX) analysis in the SEM was performed in order to characterize the oxide layers formed during fretting.

Transmission electron microscopy (TEM) was employed to study the formation of the nanocrystalline surface layers and the deformation mechanisms active during wear at different temperatures. A Philips CM 30 microscope equipped with a LaB_6-catode and a twin lens was used. For the investigation of the deformation and failure

mechanisms cross sections of the wear scars were prepared using SiC-papers down to a grain size of 2400. ¾ discs of 100 μm thickness containing the deformed zone were stamped out and dimpled in order to create a cavity below the contact zone. The final sample thickness was achieved using a ion mill Baltec Res 010. Additionally sections parallel to the scar plane were prepared in order to characterize the tribollogically modified surface layers. These parallel sections were also prepared using SiC-papers and subsequently dimpled from the side, that does not contain the wear scar, in order to increase the probability that during electro-polishing a hole appears within the wear scar. Then the side containing the wear scar was covered by a transparent plastic foil and the parallel sections were electro-polished using a Struers Tenupol machine. For electro-polishing a solution of perchloric acid (5 –10%) and ethanol was used.

4.4 Micro- and Nanohardness tests

The cross sections prepared for LM were also used for the microhardness tests. The measurements were realized in a light microscope equipped with an automatic durometer. A Vickers indenter was used with a load of 1N (HV0.01) and a hold time of 10s. Additionally nanohardness tests using a Berkovich indenter were carried out at the CrMn steel samples. Nanohardness measurements were necessary due to extremely thin contact layers, which were formed on the surface in the steel 1.4452. For the nanohardness tests a penetration depth of 0.3 μm was chosen.

4.5 X-ray diffraction studies

The wear scars were investigated using conventional X-rays and synchrotron X-rays. The synchrotron X-ray experiments were performed at the diffractometer G3, MAXIM, at the HASYLAB at DESY, Hamburg.

4.5.1 Phase analysis

The basics of the determination of the martensite content in austenitic steels is described elsewhere [FAN72, WOL72]. The quantitative analysis of the martensite fraction after friction was performed using the recorded diffractrograms of the wear scars and taking the texture in each phase into account.

The measurements were carried out using with a beam size 1mm perpendicular to the sliding direction and 2mm along the sliding direction. The difractograms were recorded for λ = 0.1790 nm in a 2θ-range from 48° to 120° with 0.02° step size. The data acquisition time was about 3s per point.

4.5.2 Profile analysis

The analyses of the X-ray reflection broadening concerning the lattice imperfections generated by friction were carried out using the JAVA-based Rietveld´s software MAUD [LUT90,LUT98,SCA94,SAH02,SAH02I]. The diffractograms are simulated by fitting structural parameters (unit cell and atomic coordinates), instrument broadening function, microstructural parameters such as crystallite size, root mean square (r.m.s.) microstrains, stacking and twin fault probabilities and the background function. The instrument broadening function was determined using a standard silicon powder with a well-known grain size distribution. All variable parameters are refined by means of an iterative least-squares procedure, in which the residual parameter is minimized [YOU93].

The Rietveld method basically consists of modeling the experimental X-ray diffraction pattern with analytical functions, which contain both the instrumental and the material specific parameters. The reflection profiles are usually described by pseudo-Voigt functions pV(x), whose intensity is directly related to the structure of each studied phase:

$$pV(x) = I_p\left[\eta C(x) + (1-\eta)G(x)\right] \qquad (4)$$

where $C(x)=(1+x^2)^{-1}$ and $G(x)=\exp[-(\ln 2)x^2]$ with $x=(2\theta-2\theta_0)/\omega$, $2\theta_0$ is the peak maximum position, 2ω the full width at half maximum (FWHM), which is assumed to be the same for both the Cauchyian (first part) and Gaussian (second part) components of Eq.(4), η the Cauchyian content of the Pseudo-Voigt (pV) function and I_p the amplitude.

Although the assumption of equal FWHM for both the Cauchyian and Gausssian components in Eq.(4) limits the applicability of the method but allows the evaluation of the relationships (after the Fourier Transform of the pV function), which establish the distribution of size effect in both the Cauchyian and Gaussian parts of the pV function [LEB00].

The profile of the X-ray diffractogram can be well simulated by a convolution equation as reported in [ENZ88]:

$$Y_C(2\theta) = [B * (I * A)](2\theta) + bkg \quad (5)$$

where * is the convolution symbol and bkg is a fourth degree polynomial function representing the background. B(2θ) describes the 'true' line broadening due to the specimen microstructure, A(2θ) the asymmetric components of the instrument peak profile and I(2θ) the symmetrical effects. B(2θ) and I(2θ) are represented by a pV function and A(2θ) = exp[-a $|2\theta_m - 2\theta_0/\cot(2\theta_0)|$].

The shape parameters ω and η from Eq.(4) for the B profile function depend on the scattering angle. These parameters are generated from the crystallite size (D) and microstrain ($<e^2>^{1/2}$) values of the sample, which are the fitting parameters, following the method used in [LUT90,CHA00].

An advantage of MAUD is its applicability to cases of anisotropy of size and strain, which lead to a (hkl)-dependence of the reflection broadening. The crystallite size (D) and the microstrain ($<e^2>^{1/2}$) are evaluated using the Popa model [POP98]. The fitting parameters correspond exactly to the variables of this model, except the value for the crystallite size, which represents the diameter of the crystallite and not the radius, and the microstrain, that is the square root of the E_i parameters reported in [POP98] (the sign of the parameter is conserved). In the present case, the equations used for crystallite size $<D_h>$ and microstrain $<\varepsilon^2>$ for the Laue group m3m (cubic) are:

$$<D_h> = D_0 + D_1K_4^1(x,\varphi) + D_2K_6^1(x,\varphi) + D_3K_6^1(x,\varphi) + ... \quad (6)$$

$$<\varepsilon_{hh}^2>E^4_H = E_1(h^4+k^4+l^4) + 2E_2(h^2k^2+k^2l^2+l^2h^2) \quad (7)$$

According to Warren [WAR69], the three kinds of planar defects, namely twin faults, expressed in terms of probability β and two deformation (stacking) faults, expressed by the intrinsic α' and the extrinsic α'' probabilities, induce a shift, an anisotropic broadening and an asymmetry of the reflection profiles as follows:

$$\Delta(2\theta) = \frac{90\sqrt{3}(\alpha' - \alpha'')\tan\theta}{\pi^2 h_0^2 (u+b)} \sum_b (\pm L_0) \quad (8)$$

$$\frac{1}{D_{eff}} = \frac{1}{D} + \frac{[1.5(\alpha'+\alpha'') + \beta]}{a h_0 (u+b)} \sum_b |L_0| \quad (9)$$

$$y_2 - y_1 = \frac{2Ab(4.5\alpha''+\beta)}{\sqrt{3}\pi(u+b)} + \frac{L}{|L_0|}\frac{1}{c_2 x_2} \tag{10}$$

$$c_2 = 1 + \left\{\frac{\lambda}{4\pi D_{eff}[\sin(\theta_0 + x_2) - \sin(\theta_0)}\right\}^2 \tag{11}$$

MAUD uses the α', α'' and β probabilities as refinable parameters. Eq.(8), (9) and (10) represent the peak shift, broadening and the asymmetry introduced due to the twin and deformation faults in a fcc structure.

The diffractograms are fitted based on the minimization of the weighted residual error (R_w) using a Marquardt least-squares program:

$$R_{wp} = \left[\frac{\sum_i w_i (I_{io} - I_{ic})^2}{\sum_i w_i I_{io}^2}\right]^{1/2} \tag{9}$$

where I_{io} and I_{ic} are the experimental and calculated intensities, respectively, and w_i (=1/ I_{io}) is the weight of experimental observations.

The goodness of fit (GoF) is evaluated by comparing R_w with the expected error R_{exp}:

$$R_{exp} = \left[\frac{N-P}{\sum_i w_i I_{io}^2}\right]^{1/2} \tag{10}$$

where I_{io} and I_{ic} are the experimental and calculated intensities, respectively, w_i (=1/ I_{io}) and N are the weight and number of experimental observations, and P is the number of fitting parameters. This leads to the value of goodness of fit:

$$GoF = \frac{R_w}{R_{exp}} \tag{11}$$

The refinement is performed until the convergence is reached and the value of the quality factor (GoF) approaches 1.

The SFE and the dislocation densities are evaluated from the microstrains and stacking fault probabilities determined by the Rietveld refinement procedure [WER83,SCH75], as follows:

$$SFE = \frac{K_{111}\omega_0 G_{(111)} a_0 A^{-0.37}}{\pi\sqrt{3}} \frac{\left\langle \varepsilon_{50}^2 \right\rangle_{111}}{\alpha} \quad (12)$$

where $<\varepsilon_{50}^2>_{111}$ is the microstrain along the <111> crystallographic direction, α is the stacking fault probability and

$K_{111}\omega_0$ = proportionality constant

$G_{(111)}$ = shear modulus in the (111) fault plane, = $1/3(c_{44}+c_{11}-c_{12})$

a_0 = lattice constant

A = Zener anisotropy = $2c_{44}/(c_{11}-c_{12})$, and

c_{ij} = elastic stiffness coefficients

$$\rho = \frac{48\pi\alpha(SFE)}{(K_e + K_s)a_0^2 d_{111}} \quad (13)$$

where ρ is the dislocation density, d_{111} is the interplanar spacing,

$$K_s = \left\{ \frac{c_{44}}{2}(c_{11} - c_{12}) \right\}^{1/2}$$

and

$$K_e = (c_{11} + c_{12}) \left\{ \frac{c_{44}(c_{11} - c_{12})}{c_{11}(c_{11} + c_{12} + 2c_{44})} \right\}^{1/2}$$

4.5.3 Texture analysis

The experimental texture analysis using a monochromatic beam is based on the determination of reflection intensities for discrete points in the laboratory coordination system using equally spaced steps in the Eulerian space. The entire Eulerian space can be mapped by turning the sample around the azimuthal angle φ and the tilting angle ψ (Fig.8a).

For the texture analysis the intensity of each reflection should be evaluated over the largest angular range possible. Due to the Friedel´s law, whereby the intensity of the secondary beam is the same for positive and negative directions of measurement, only the half angular zone must be evaluated [HEL96]. However experimental obstacles lead usually to smaller angular regions reachable and as a result only incomplete pole figures can be measured. The intensity distributions are displayed in pole figures of each reflection measured. In pole figures the poles of a specific crystal

direction <hkl> are specified with respect to the sample coordinates in the stereographic projection. A pole figure is proportional to the volume fraction of all crystallites, whose crystallographic direction is parallel to the sample vector.

Similarly preferential orientations can be described by inverse pole figures, i.e. specifying the poles of the sample coordinate system with respect to those of the crystal coordinate system in the stereographic projection.

In the present work texture analyses were carried out using a ψ-diffractometer equipped with a position sensitive detector (PSD). In the wear scars the γ_{111}, γ_{200} and γ_{311} as well as the α_{110}, α_{200} and α_{211} reflections, in case of the metastable steel 1.4301, were considered. The measurements were performed in a range of $0 \leq \varphi \leq 350°$ with steps of $\Delta\varphi = 10°$ and $0 \leq \psi \leq 75°$ with steps $\Delta\psi = 5°$. Conventional CoK_α-radiation (λ=1.7889 Å) with a round collimator (ϕ = 1mm) was employed. Sample time amounted to 50s per point.

The software ,,ODF-Analysis'' [BUN93] developed by the working group Textures at the TU Clausthal was used for the data evaluation. From the recorded intensity distributions measured pole figures are displayed. Using series of generalized spherical harmonics complete pole figures as well as inverse pole figures could be calculated.

4.5.4 Residual stress analysis

For residual stress analysis the $\sin^2\psi$-method was chosen. In the austenite the residual stress values were determined using the (311) reflection, in the martensite measurements were carried out on the (211) reflection. A wavelength λ = 0.1790 nm with a beam size of 1X1 mm^2 was employed at HASYLAB. Sample time amounted to about 5s per point. The ψ-angle was varied between 0° and 75° ($\sin^2\psi$=0.933) and four φ-angles were used to simulate positive and negative ψ-angles. The data evaluation was carried out using the Mathematica routine ,,Reflexlagenbestimmung von Röntgeninterferenzen sowie Spannungsanalyse mittels sin²(psi)- Methode'' developed by C. Genzel.

The $\sin^2\psi$-method is the traditional technique for analyzing near surface stresses with X-rays [MAC61,NOY87,HAU97,FIT03]. The method uses the linear variation of the d-spacing with the square of the sine of the angle between any two principal directions, when the out-of-plane stress component σ_{33} is negligible within the penetration depth of the radiation used.

If additionally the principal directions are assumed correctly, the fundamental diffraction strain relationship is simplified to:

$$\varepsilon_{\varphi\psi} = \frac{d_{\varphi\psi} - d_0}{d_0} = \frac{1}{2} S_{2(hkl)} \sigma_\varphi \sin^2\psi + S_{1(hkl)} (\sigma_{11} + \sigma_{22}) \qquad (14)$$

where $\varepsilon_{\varphi\psi}$ is the strain along the sample direction given by the azimuthal angle φ and the tilting angle ψ, d_0 is the stress-free lattice spacing and ½ $S_{2(hkl)}$ and $S_{1(hkl)}$ are the x-ray elastic constants.

The slope of the measured d-spacings will be proportional to the stress σ_φ. In case of a biaxial stress state, d_0 is only a multiplier in the slope and its accurate value is not necessary to determine the stress σ_φ. Any uncertainty in d_0, easily determinable to a fraction of one percent, is reflected to the same proportion in the uncertainty in stress and is generally negligible in comparison to other uncertainties. The principal stress components σ_{11} and σ_{22} are then evaluated from the slope of the $\varepsilon_{\varphi\psi}$ vs. $\sin^2\psi$-curve for measurements in the azimuthal angles φ = 0° and 90° (Fig.8b).

5 Results

5.1 Sliding Friction

5.1.1 Wear Resistance

The wear resistance during sliding friction tests in LH_2 was evaluated by means of the wear scars created on the counterbody. These worn areas produced on the Al_2O_3-balls were chosen for the evaluation of the wear amount, since on the steel specimens the scar depths are very small (comparable to the roughness of the polished surface) and the scar widths may lead to an erroneous interpretation due to the material transfer between disc and counterbody during adhesive wear. The error bars give the standard deviation between the diameters measured along and perpendicular to the sliding direction. Fig.9 shows the variation of the scar widths on the ball with temperature and environment for the alloys investigated. At RT the low and intermediate alloyed CrNi steels 1.4301 and 1.4439 exhibit a lower wear resistance than the high alloyed CrNi steels 1.4876 and 1.4591 and the high N-alloyed CrMn steel 1.4452. At 77 K the width of the wear scars for all steels investigated remains nearly the same. However, a further decrease in temperature to 20 K and 4.2 K reduces the scar widths, except in case of the Mo- and N-free alloy 1.4876 at 20 K in LH_2, where an appreciable loss of wear resistance is observed.

The influence of the loading conditions on the scar width was studied at 20 K in LH_2. Fig.10 displays the variation of the scar widths with the tribological stress conditions for the different austenitic steels. Results reveal that for mild tribological stressing (F_N = 5 N, v = 0.06 m/s) the wear resistance of all investigated alloys is nearly the same. An increase of the sliding speed (F_N = 5 N, v = 0.2 m/s) leads to a reduction of wear in all N-alloyed steels and to a linear increase of wear in the N-free 1.4876. On the other hand, distinct wear performances for each investigated austenitic steel appear at more severe stress conditions (F_N = 10 N, v = 0.2 m/s). The metastable CrNi steel 1.4301 and the CrMnN-steel 1.4452 with the lowest SFE present the best wear resistance The second best wear performance is found for the Mo-alloyed steel 1.4439 with about 0.17 % N and moderate SFE. For these three steel grades (1.4301, 1.4452 and 1.4439) the increase of normal force and sliding speed does not affect material removal. A high SFE leads clearly to a loss of wear resistance. The

high alloyed steel 1.4591 with 0.39 % N exhibits an intermediate wear performance, whilst the Ni-free steel 1.4876 appears with the broadest scar.

5.1.2 Surface Morphology

Fig.11 displays a cross-section of the wear track produced in the steel 1.4301 after friction in LH_2. In all investigated alloys the tribologically modified zone is characterized by an extreme deterioration.

Fig.12 shows typical images of the topography of the wear scars. By an adhesive wear mechanism, particles are detached from the tribologically modified zone, then transferred to the counterbody and finally re-transferred to the sample surface. The wear particles are generated as soon as the mechanical strength reaches its limit during the shear deformation of the surface. Crack formation could not be detected even at the lowest temperature, i.e. LHe (4.2K), in all investigated alloys.

In liquid hydrogen the deformation behavior in the contact zone appears to be different, as shown in Fig.13. Crack formation is observed in particles deposited as well as in the worn matrix. The crack density depends on the alloy and the loading conditions. The materials 1.4452, 1.4301 and 1.4439 with low/intermediate SFE exhibited more severe crack formation than the high SFE alloys 1.4876 and 1.4591. LM studies of cross-sections (Fig.14) revealed that these cracks propagate about 5-6 μm across the deteriorated contact layer and are deflected at the interface between contact layer and bulk material. Beneath the surface a crack network is formed, which leads to the breakout of surface material.

Systematic SEM studies of the wear scars were carried out in order to evaluate the effect of the stress conditions and the chemical composition on the cracking process for the different austenitic alloys. Fig. 15-17 display the worn surface of the austenitic steels 1.4452, 1.4876 and 1.4591 after friction at different conditions. In 1.4452 cracking occurs at all loading conditions and is intensified by increasing loadings. In turn only very few cracks are formed in 1.4876 at the slightest applied tribological loading of 5 N and 0.06 m/s. Heavier loading does not increase the crack formation but rather suppresses it. The steel 1.4591 is more sensitive to cracking than 1.4876

at 5 N and 0.06 m/s loading but, similarly to the latter, presents reduced cracking under heavier tribological loading.

The in-depth extension of the strengthened near-surface-zone in the different austenitic alloys after friction in LH_2 was evaluated by means of micro- and nanohardness tests. Using microhardness tests the hardened zone formed in the steel 1.4452 could not be characterized. Fig.18 shows the hardness depth profiles for the steels 1.4452, 1.4301, 1.4439 and 1.4591 after tribological loading with 5N and 0.06 m/s. The depth of the hardened zone amounts to about 50 μm for the CrNi steels (1.4301, 1.4439 and 1.4591) and is clearly thinner for the CrMnN steel (1.4452) (app. 5 μm).

5.1.3 Microstructural Changes

Systematic microscopy studies on the steels 1.4301 and 1.4439 after friction were carried out in order to evaluate the influence of the temperature and environment on the deformation mechanisms as a function of the SFE. Fig.19-20 display LM images of the steels 1.4301 and 1.4439 after friction at RT and in cryogenic environments. In all alloys investigated the top zone of the near surface microstructure consists of a strongly layered structure, which differs completely from the initial microstructure of the parent material. This zone is about 10-15 μm thick. Below the top contact zone a deformed microstructure of about 50 μm depth is built up. In the deepest portions of this friction affected zone twinning can be observed depending on the test temperature and the alloy. Austenitic steels with low SFE (1.4301 and 1.4452) are deformed by twinning already at RT, whilst in the alloys with high SFE (1.4439, 1.4876 and 1.4591) twinning is observed only at low temperatures. TEM micrographs reveal that in the material 1.4439 with medium SFE mostly dislocation gliding occurs at RT (Fig.21a). On the contrary in the alloy 1.4301 with low SFE twinning can be clearly observed at RT using LM (Fig.19a).

LM investigations on samples worn at cryogenic temperatures reveal that in all investigated steels (1.4301 and 1.4439) the role of twinning in the deformation process increases with decreasing temperature. Fig. 20b,d show LM micrographs of the steel 1.4439 after friction in cryogenic environments. Massive twin blocks are observed after wear in LH_2, as exemplified in Fig. 20c and 21b. This influence of

hydrogen on the deformation process can be also visualized in the shape of the X-ray reflection profiles from the wear scar (Fig. 22). Twinned Zones cause an asymmetric broadening of reflection profiles, as shown in Fig. 22 after wear of the steel 1.4439 in LH_2.

The broadening of the austenite reflection profiles in the steel 1.4439 was quantitatively analyzed using a Rietveld refinement procedure. Fig.23 shows the temperature dependence of the SFE and of the ratio between twinning probability (β) and dislocation density (ρ). The SFE decreases linearly and the ratio between twinning probability and dislocation density increases exponentially with decreasing temperature. At 20K in LH_2 an additional SFE decrease along with an increased β/ρ ratio are observed.

TEM investigations on the materials 1.4301 and 1.4439 worn in LH_2 (Fig.24) have shown that microcracks are formed in austenitic zones, in which numerous intersecting slip bands and glide-twin interactions occur. In case of the metastable alloy 1.4301 the martensite nanocrystallites are only penetrated by cracks during their propagation and the crack initiation occurs within the embrittled austenite.

In order to clarify the mechanisms of cracking in LH_2 and its variation with the loading conditions, the broadening of X-ray reflection profiles in the alloys 1.4452 and 1.4876 was also quantitatively analyzed using a Rietveld refinement procedure regarding lattice constant (a), SFE, dislocation density (ρ) and twinning probability (β). Results are shown in Fig. 25-26. The different loading conditions were also displayed as the energy rate (E_t) introduced in the worn surface, which is given by $E_t = F_N$ v. The hydrogen uptake can be visualized by means of an expansion of the unit cell. The lattice constant is determined by the Rietveld refinement procedure and represents a mean value for several reflections at ψ=0°. In both alloys a marked decrease of the lattice constant indicates that the hydrogen solubility in the austenitic lattice decreases severely with increasing loading. In the steel 1.4452 with a very low SFE the hydrogen uptake does not affect the SFE, which is already extremely low at 20K (0.1 - 0.85 mJ/m^2). The twinning probability rises considerably when compared to the dislocation density at high energy rates. Contrary to the steel 1.4452, in the high-alloyed steel 1.4876 with a high SFE, the decreasing hydrogen uptake with increasing energies markedly increases the SFE.

For all studied steels TEM investigations of the top surface layer show clearly the formation of heavily fragmented and nanostructured layers after friction in all investigated environments (Fig.27). Texture formation within the contact zone during friction can be also observed. Dark field images using the scattered background between two arbitrary Debye-Scherrer rings did not reveal any amorphous region. Fig. 27c shows a heavily twinned region within the contact zone in the alloy 1.4301 after friction in LH_2

5.1.4 Strain Induced Phase Transformation

All austenitic steels after sliding friction tests in LH_2 were investigated by X-ray diffraction concerning possible strain induced martensitic transformation. Results displayed in Fig. 28 show that the austenitic microstructure in the CrNi steels 1.4439, 1.4876 and 1.4591 is not susceptible to phase transformation during wear processes. The stability of the austenite in these so-called stable alloys is not affected by temperature, environment, normal forces or sliding velocities.

In contrast to the high alloyed CrNi steels, the metastable alloy 1.4301 exhibits a significant martensitic transformation already after stressing at RT. The presence of δ-ferrite, which may influence the accurate determination of martensite in a X-ray diffractogram, could not be detected within the parent material. The wear process of 1.4301 was monitored at RT during and after the running-in period (Fig.29). A measurable martensite content is visible already after a few loading cycles. The phase transformation within the wear scar proceeds with increasing sliding distance. However, after 500 cycles a maximum martensite fraction is observed followed by a steep decrease up to 700 cycles, after which the martensite content remains nearly the same. The martensite volume fraction within the wear scar increases again after the running-in regime and reaches substantially higher values than in the running-in period (7700 and 10000 cycles). However, a steady state between the strain induced phase transformation and the wear rate does not seem to be achieved, since the martensite content measured still oscillates considerably after the running-in regime (Fig.29).

Fig.30 displays the dependence of the martensite volume fraction on the test temperature in the metastable steel 1.4301 for a normal force F_N = 5 N and a sliding

velocity v = 0.2 m/s. The martensite volume fraction is higher at 77 K in LN_2 than at RT. This is due to an enhanced metastability of the austenitic microstructure at lower temperatures. By further cooling down to 20 K in LH_2 a marked reduction of the martensite content within the wear scar is observed. Cooling down to 4.2 K in LHe does not change the transformed volume fraction.

In LH_2 the normal force and sliding velocity were varied in order to study their influence on the phase transformation (Fig.31). Increased normal forces led to more intense martensitic transformation. Also slower sliding motions promoted a slightly increased martensite fraction. This is in agreement with previous investigations [ASS04] by magnetic inductive methods, where a significant variation of the martensite fraction with the sliding velocity could not be determined.

Contrary to the high-alloyed CrNi steels 1.4876 and 1.4591, where no martensitic transformation occurred at all, and the CrNi steel 1.4301 where an γ/α'-transformation occured, in the CrMnN steel 1.4452 a γ/ε-martensite transformation was observed after friction in LH_2 under F_N = 10 N, v = 0.2 m/s (Fig.32). At RT no phase transformation was observed.

The ε-martensite formed is very inhomogeneously distributed across the wear scar and strongly textured, i.e. only ε_{101} and ε_{103} reflections appear very intensive and the other ones are not observed. The texture of the ε-martensite is due to the inheriting of the texture from the austenite, which was formed by plastic deformation in the wear scar. The inhomogeneous spatial distribution and the strong texture formation induce very high uncertainties in the phase analysis. Thus, a quantitative analysis of the formed ε-martensite content could not be performed.

5.1.5 Texture Formation

Texture analysis of the wear scars using X-ray diffraction showed the influence of the active deformation mechanisms and, consequently, of temperature and environment on texture formation. In all alloys investigated a similar texture formation and evolution with temperature was observed.

At initial stages of the wear process at RT, a (211)<111>-rolling texture is built up after 1200 cycles in the austenite (Fig.33). In addition the <111>-crystallographic direction appears in the inverse pole figures as well as during TEM sessions as a texture component along the radial scar direction (Fig.33-34a).

With increasing number of cycles, the texture in the austenite turns into a <111>-fiber component along the scar normal direction (Fig.35).

In turn a <210>/<221>-double fiber texture is formed in the martensite along the scar normal direction (Fig.36).

At cryogenic temperatures the development of a (110)<111>-rolling texture is observed in the austenite (Fig.37).

On the other hand, at low temperatures the martensite inherits the texture formed in the austenite and a <111>-fiber texture along the scar normal direction (Fig.38) is built up according to the orientation relationship between martensite and austenite. Another possible preferential orientation in the martensite at cryogenic temperatures was observed during TEM studies. Fig.34b reveals a <110>-texture component along the sliding direction. Since TEM enables only very local microstructure analysis and the texture analysis using X-ray diffraction covers large and representative gauge volumes, their results are not always comparable.

Fig.39 summarizes the results on texture formation and its evolution with the temperature.

5.1.6 Internal Stresses

After sliding friction compressive stresses are built up. The internal stresses in the martensite in the metastable alloy 1.4301 (Fig.40a) depend on the scar direction. Higher stress values arise along the radial scar direction. For the untransformed austenite only slightly increased compressive stresses appear along the radial scar direction. Furthermore lower stresses appear after friction in LH_2. For all stable steels the internal stresses in the austenite are rather rotation-symmetric (Fig.40b).

5.2 Fretting

5.2.1 Wear Resistance

The influence of the relative air humidity on the wear performance was evaluated by means of worn areas on the steel discs determined by SEM inspection. Results (Fig.41) reveal that for all investigated CrNi steels the wear amount decreases with increasing relative air humidity. The evaluated worn areas stem from single length measurements of the ellipsoidal calotte axis and consequently no error bar can be given. The wear performance of the four different CrNi steels are very similar at each different air humidity.

5.2.2 Surface Morphology

Reciprocating sliding wear at RT in air was employed in order to investigate the effect of the relative air humidity on the wear behavior. Oscillating sliding friction increases the mechanical activation of the worn surface and, consequently, speeds up the tribochemical oxidation at the contact zone.

Fig.42 displays worn surfaces in dry and humid air for the steel 1.4301. In dry air a strongly deteriorated contact surface is observed within the wear scar. The wear mechanism at 3% and 50% relative humidity is predominantly adhesive, as during unidirectional sliding friction. Particles are detached from the worn surface when the shear strength is achieved and then transferred from the counterbody back to the metallic surface. In 100% humid air these features are not clearly visible and on the worn surface a tribochemically smoothed layer can be observed. EDX-analysis (Fig.42b,c) revealed qualitatively the presence of oxide layers in certain portions of the wear scar only in samples worn in humid air.

5.2.3 Strain Induced Phase Transformation

The influence of air humidity on phase transformation was studied by X-ray diffraction. As expected from the results of the sliding friction tests, only the conventional low alloyed steel 1.4301 forms martensite in the wear scars after oscillating friction at RT. Fig.43 shows the variation of the martensite content in the alloy 1.4301 with the air humidity. A significant reduction in the volume fraction of martensite with increasing air humidity is observed.

In addition synchrotron X-ray diffraction studies with high spatial resolution revealed that after oscillating friction in humid air traces of ε-martensite are still present in the wear scar (Fig.44).

5.2.4 Internal Stresses

Results of the internal stress analysis after oscillating friction tests (Fig.45) show again the influence of the relative air humidity on the wear process. In humid air lower compressive stresses are introduced into the contact zone.

6 Discussion

6.1 Wear Behavior

Stainless CrNi- and CrMn-steels are materials currently employed in cryogenic applications, i.e. in liquid gaseous environments and in superconductive magnetic systems. Due to their fcc-crystal structure these steels show sufficient toughness down to temperatures close to zero Kelvin. The relatively low mechanical strength of austenitic steels, such as the alloy CrNi18-8, can be enhanced by adding Mo and N.

Here the temperature dependence of the wear resistance was investigated for austenitic steels. At RT the CrNi steels 1.4301 and 1.4439 with low and intermediate SFE are less wear resistant than both high alloyed CrNi steels (1.4876 and 1.4591) and the high N-alloyed CrMn steel (1.4452). The SFE is known to affect the wear resistance of metallic materials [RIG77,WER83]. It was suggested that the role of the SFE is connected to the ease of developing a cell structure is developed within the contact zone of the wear partners. In materials with a high SFE, tangled cell walls are easily formed since cross-slip readily takes place. Conversely, a low SFE assists planar slip, which inhibits cell wall formation up to very large strains. According to this model, cell walls may serve as subsurface pathways for cracks propagating parallel to the surface. This results eventually in the formation of wear debris and increased wear. Thus, higher wear resistance should be expected for materials with low SFE.

However, this is opposite to the results obtained at RT. In the present case the enhanced deformation capability of materials having high SFE seems to be the most relevant factor. This trend was already reported elsewhere [HSU80,WER83]. At RT the considerable wear rate, when compared to the amount at cryogenic temperatures, suggests the generation of high surface strains during friction at RT. Consequently at RT the shear strength of lower SFE alloys is reached earlier and a more intense material removal occurs.

The relative air humidity was another parameter studied at RT. For all steels investigated increasing air humidities led to less wear. In LN_2 the investigated alloys behave similarly to RT. Further decreasing temperatures lead to reduced wear due to an increase in mechanical strength for all steels.

LH_2 is considered as a special environment. It has been shown that hydrogen can cause a reduction of ductility and fracture stress not only in iron and steel but in many materials. Analysis of the wear tests in LH_2 reveals that hydrogen does not affect significantly the wear resistance of the steels investigated, except the Mo- and N-free alloy 1.4876. For the latter a marked increase of the scar width at 20 K in LH_2 indicates an H-induced loss of wear resistance due to its lower mechanical strength when compared to the other materials considered.

In LH_2 the loading conditions were varied in order to study their effect on wear resistance. At low deformation energies (F_N = 5N, v = 0.06 m/s) the still high toughness of all investigated steels at low temperatures meets the requirements for a satisfactory wear performance. With increasing sliding speeds (F_N = 5N, v = 0.2 m/s) the lower mechanical strength of the Mo- and N-free alloy 1.4876 leads to a pronounced loss of wear resistance. All other austenitic steels present a slightly enhanced wear performance at high sliding speeds. It has been shown [TOM90,TOM98,OBS91] that increased strain rates, i.e. during fast sliding motions, applied on austenitic steels at low temperatures may drastically change the failure mode from cleavage-like to ductile. A detailed study [OBS91] of this low temperature softening caused by an increase of the strain rate revealed conclusive evidences that the effects of local heat generation are negligible. The increased ductility arises from the breakdown of Lomer-Cottrell locks by a critical number of edge dislocations in strongly localized slip planes. Therefore the slightly increased wear resistance at high sliding speeds could be attributed to an enhanced material plasticity.

On the other hand, under severe stress conditions (F_N = 10N, v = 0.2 m/s), the chemical composition seems to determine the wear resistance and low SFE´s led to the best wear performance. These results suggest in case of the metastable alloy 1.4301 an important role of the strain hardening by martensite formation on the wear performance.

In addition a positive effect of Mo- and N-alloying in CrNi steels can be observed. Moderate Mo- and N-contents are known to increase the yield strength while sufficient toughness remains [STA01,SCH98]. This explains the good wear resistance of 1.4439 at cryogenic temperatures.

On the contrary a high N-content (1.0%) in the CrMn steel can result in loss of ductility. Using impact tests [TOM98I,HAR90] could already show that high N-additions result in brittleness in austenitic steels even at RT. In Ni-free CrMn steels, such as the alloy 1.4452, this was observed if the N-content amounts to about 1 mass %. The formation of narrow slip bands, accumulation of shear strain within the narrow band due to the difficult activation of the out-of-plane secondary slip and weakening of the slip band by accumulated dislocations to the extent of its final separation (cleavage-like fracture) rank among the many attempts to clarify the mechanism of N-induced brittle fracture [TOB88,LIU98]. Furthermore a decisive role of twinning was suggested in [MÜL94,MÜL97]. If the dislocation density is sufficiently high, the stress relaxation at the crack tip is provided by dislocation slip and the tip can blunt. N as well as Mn shift the onset of twinning to lower strains, where the dislocation density is still low and a critical stress for brittle fracture may be achieved before the crack tip blunts. However, the increased mechanical strength of the worn surface layer seems to be responsible for the best wear resistance of the CrMnN steel 1.4452.

The worn surfaces inspected by means of SEM revealed a satisfactory ductility of all investigated alloys down to temperatures in LHe (4.2K). Contrary to the other environments studied, in LH_2 the formation of brittle crack networks is visible. An appreciable decrease of the SFE along with a very high yield strength and texture hardening favor cracking at the worn surface during friction in LH_2 by the pressure buildup mechanism [HÜB03,HÜB04,PIN03]. Crack formation after friction in LH_2 is observed within the wear scars of all studied alloys at mild tribological loading (F_N = 5N, v = 0.06 m/s). Increasing sliding speeds as well as increasing loadings induce a more intense cracking in the steels with low and intermediate SFE (1.4452, 1.4301 and 1.4439). High SFE´s led to an unexpected behavior. In the high-alloyed CrNi steels 1.4876 and 1.4591 the cracking density is clearly lower at higher deformation energies (increased speed and loads) and in case of 1.4876 almost no cracks can be detected. This suggests that in case of 1.4876 and 1.4591 the more pronounced deformation and severe loading conditions do not enhance hydrogen uptake but likely facilitate hydrogen release. It is assumed that hydrogen is continuously driven out and it is not soluted in the austenitic crystal lattice.

The wear induced crack formation in almost all worn steel surfaces indicates that, even though no strain induced phase transformation takes place, a hydrogen induced embrittlement may occur in the so-called stable austenitic steels. However, the embrittlement is not necessarily connected to a low wear resistance at cryogenic temperatures. As shown in Fig. 10, 1.4876 and 1.4591 exhibit unsatisfactory wear performances but are less embrittled in presence of hydrogen. On the contrary the metastable 1.4301, the steel 1.4439 and even the alloy 1.4452 with the best wear performance reveal a very high crack density. These cracks propagate only within the contact layer (5-6 μm) and do not penetrate the bulk material. Therefore, they do not seem to influence the wear behavior and could affect the lifetime of machine components only if external tensile stresses act additionally on the tribo-system.

Furthermore the strengthening of the considered alloys within the near surface zone, evaluated by means of micro- and nanohardness tests, follows the expected trend, that hardening rate increases with decreasing SFE (1.4591 < 1.4439 < 1.4301 < 1.4452). The concentration of the entire deformation energy within a 5 μm layer in the steel 1.4452, as revealed by the hardness tests, leads to a marked deterioration of the worn surface and explains the very high crack density. This reflects once again the pronounced increase of mechanical strength accompanied by a significant loss of ductility in the CrMnN steel 1.4452 at cryogenic temperatures, as already described for other FeCrMnN alloys in [GAV99].

6.2 Effect of chemical composition, temperature and environment on martensitic transformation

Pre-requisite for satisfactory toughness values at cryogenic temperatures, such as in LH_2 and LHe, is a stable austenitic microstructure. The formation of strain-induced α´-martensite reduces the toughness and the corrosion resistance. In addition the ferromagnetic α´-martensite is easily magnetized. The lower the magnetization of the steel, the less heating is induced by eddy-currents and the smaller are the mechanical forces induced by the magnetic fields.

The stability of the austenite at low temperatures is determined by the chemical composition. The elements Ni, Mn, C and N are most effective in stabilizing the austenite but are supported by the ferrite forming elements Cr and Mo to a lesser

extent as can be derived from the Schaeffler diagram (Fig.2). An important parameter for the stability of the austenitic microstructure is the martensite start temperature M_S. The influence of the alloying elements on the M_S-temperature is usually described by empiric regression equations, such as [WER85]:

$$M_S\,[°C] = 1305 - 1665\,(\%C + \%N) - 28\,(\%Si) - 33.5\,(\%Mn) - 41.5\,(\%Cr) - 61\,(\%Ni) \quad (15)$$

All investigated high-alloyed CrNi steels showed a very stable austenitic microstructure. Even in LHe no phase transformation was observed. However, it must be pointed out, that, though an increasing Ni-content suppresses the formation of strain induced α'-martensite, the paramagnetic austenite may transform to antiferromagnetic or ferromagnetic austenite depending strongly on the Ni-content, as shown in Fig.3. Thus, the high alloyed CrNi steels 1.4876 and 1.4591 are not usable in non-magnetic applications. On the other hand the alloy 1.4439 with an intermediate Ni-content exhibits a high Néel temperature T_N, below which the magnetic susceptibility decreases, and fulfills this way the requirements for a cryogenic non-magnetic steel.

Only the alloy 1.4301 presented a strain-induced phase transformation. In this steel martensite forms already after friction at RT. The wear process in the steel 1.4301 was monitored at RT, starting in the running-in period. It could be shown that already during the first tribological cycles plastic deformation leads to a phase transformation within the wear scar. With increasing deformation the martensite fraction grows up to a maximum, after which the brittle martensite starts being preferentially removed from the contact surface. A steady state between the strain induced phase transformation and the wear rate is not achieved even in later stages after the running-in regime.

The volume fraction of strain induced martensite formed within the worn layer in the steel 1.4301 is a function of the service temperature as well. On cooling from RT down to cryogenic temperatures the martensite content increases and finds its maximum about 77K in LN_2. With further cooling down to 20 K in LH_2 the martensite content decreases steeply and remains nearly the same for 20 K and 4.2 K. This behavior can be attributed to changes in distinct material properties at cryogenic temperatures. First, the paramagnetic austenite in the steel 1.4301 transforms in the

ferromagnetic α'-martensite below the martensite start temperature M_S (about 150 K) but with further cooling below T_N (range between 20 and 4 K) an antiferromagnetic austenite may build up [PEP92]. Another effect is the stepwise increase of mechanical strength observed at temperatures below 70 K, which contrary to the temperature effect inhibits the strain induced formation of martensite. Seeger [SEE55] has proposed that at very low temperatures, e.g. between 100 and 50 K for other austenitic steels [NYI93,GAV98], the generation of vacancies by jogs at screw dislocations determines the yield stress of metals with low SFE (see Fig.46-47). Seeger named the following three mechanisms, which may contribute to the variation of the yield stress with temperature in fcc crystals at temperatures lower than these ones when selfdiffusion occurs:

- interaction between gliding edge dislocations and a forest of dislocations threading the slip plane;
- interaction between gliding screw dislocations and the same forest;
- thermally activated generation of vacancies by jogs in screw dislocations.

At sufficient low temperatures selfdiffusion and therefore dislocation climbing during the deformation time are unlikely. The jogs that are formed in the intersection of gliding dislocations leave vacancies or interstitials behind them. Since the energy necessary to add a vacancy to the end of a row of lattice defects, generated by a gliding jog, is about one order smaller if compared to the case of interstitials, the generation of vacancies is a preferential controlling mechanism for the yield stress in fcc crystals at low temperatures (Fig.46). In case of materials with low SFE the gliding dislocations are extended. At the point of intersection (the position of a jog) the SF forms a constriction (Fig.47). After the generation of a vacancy, the jog and the constriction move away, whilst the vacancy remains attached to one of the partial dislocations decreasing the activation energy by an interaction energy between dislocation and vacancy. Therefore the lower the SFE, i.e. the more separated the partial dislocations, the higher the applied stress has to be in order to form a constriction of the dislocations. Fig.48 represents schematically the effect of temperature on the tensile properties of the austenitic steel Cr25Ni15N0.35 [NYI93I]. This stepwise increase of mechanical strength hampers plastic deformation at extremely low temperatures and consequently lower martensite contents are generated at 20 and 4.2 K when compared to 77 K.

Not only the test temperature affected the strain-induced martensite content generated in the wear scar, but also the tribological loading. Increased forces induced a more intense martensitic transformation. On the other hand, an unexpected trend was observed when varying the sliding speed. Slower motions produced slightly higher martensite volume fractions. Since a steady-state between the martensitic transformation and the wear rate is not achieved, a lower martensite content at higher velocities can be explained by a more severe removal of martensite from the contact zone at higher rotation frequencies.

Fretting was used to study the influence of the relative air humidity at RT on the phase transformation. Measurements of the contact resistance between the two sliding bodies [HÜB02,ASS04I] have shown that an oxide layer is formed during oscillating sliding friction. In case of high air humidities the polar water molecules are strongly adsorbed on the metal surface and the tribooxidation is hampered [GRO90]. Consequently the oxide layer is thicker in dry than in humid air. In turn ex-situ EDX-analysis indicated qualitatively the presence of oxides only for samples tested in 100% relative air humidity. This suggests that the thick layer in dry air is more easily removed due to its brittleness and lower adhesion as reported in [OH99]. The ε-martensite is a result of an uncompleted martensitic transformation and could be observed only after wear in 100% humid air. The internal stresses are also higher in the samples tested in dry air. These observations confirm once again the shielding effect of thin oxide layers, which are built up in humid atmospheres. Therefore, the contact zone undergoes more severe plastic deformation and martensitic transformation in dry than in humid air.

6.3 Microstructural deterioration

During deformation of austenitic (f.c.c.) steels dislocation glide occurs exclusively on the (111) planes. In case of high SFE, i.e. a small separation distance between partial dislocations, the dislocations are able to change their slip planes by cross-slip and at high strain levels the formation of dense dislocation walls is observed. On the other hand, for alloys with a low SFE, cross-slip is hindered by the large separation of the partial dislocations and, therefore, the dislocations build planar arrays on their primary (111) slip planes. Furthermore twinning [CHR95] is another deformation mechanism, which competes with dislocation slip. In general this process is favored

by low SFE, but may be also activated to accommodate deformation, specially at high strain rates and at low temperatures.

The microstructure studies by LM and TEM confirmed that in the intermediate and high alloyed CrNi steels (1.4439, 1.4876 and 1.4591) with medium/high SFE dislocation gliding is the unique deformation mechanism activated during friction at RT, whilst in case of the low alloyed 1.4301 twinning occurs as well. With decreasing temperature twinning plays increasingly a role in the entire deformation process in all studied alloys.

An abrupt increase of twinning is clearly observed during friction in LH_2. The twin density in presence of LH_2 at 20 K is even higher than after wear in LHe. Hydrogen can be easily absorbed due to the generation of numerous lattice defects at the worn surface and is known to lower the SFE of the austenite [HOL68,PON97] by pair formation within the faulted zone [HER98,JUA02]. The strong tendency of hydrogen atoms to bond finds a very favorable situation in the neighbour octahedral interstices of the HCP phase, which exists within a SF. The large SFE decrease induced by small hydrogen pairs concentration is attributted to the huge H-H binding energy. An additional decrease of the SFE along with a local increase of stresses [ZAP47] or enhanced mobility of dislocations [ROB01] by hydrogen uptake within the contact zone may assist a more intense twinning.

X-ray diffraction studies suggest once again that the absorption of hydrogen during friction at 20 K leads to an additional decrease of the SFE along with a marked increase of twin faults in comparison to dislocation lines. Asymmetric diffraction profiles appear after wear in LH_2. The simulation of the X-ray diffraction profiles using the Rietveld refinement procedure shows clearly, that the SFE increases linearly with the temperature, as expected, by an amount of 0.11mJ/m^2 per Kelvin. Similar results were reported in [REM77,LAN71], where the SFE increase with temperature in FeMnCrC- and FeCrNi-alloys was found to amount 0.08 mJ/m^2 per Kelvin. However, at 20 K in LH_2 the SFE evaluated is lower than predicted by the linear relationship with the temperature. At the same time the ratio between the twinning probability and the dislocation density increases exponentially with decreasing temperature but at 20 K in LH_2 an additional increase is also observed.

In polycrystals at RT and with higher SFE, dislocation slip, accumulation, intersection, tangling and spatial rearrangement by high deformation levels and strain rates cause grain subdivision [WU02,TAO02]. This could be observed during TEM investigations of the top surface layers produced at RT (Fig.27a).

At cryogenic temperatures and lower SFE twinning is also strongly related to the formation of a nanocrystalline microstructure [ZHA03]. Diffraction patterns of the top surface layer indicate that the formation of rhombic blocks by twin-twin intersection leads to grain refinement and the formation of martensite.

The additional decrease of SFE along with the pressure buildup mechanism by hydrogen absorption seem to be correlated with the cracking process during tribological loading in LH_2, as reported in previous works [HÜB03,HÜB04,PIN04II]. The influence of the loading conditions on the crack formation during friction in LH_2 was investigated. SEM studies revealed that in higher SFE materials the cracking intensity decreases markedly with increasing deformation energies. X-ray diffraction was employed to explain the mechanisms of crack formation. The lattice constant decreases with increasing deformation energies for both materials analyzed (with low and high SFE). This implies that H-uptake decreases with severe increases of loading, as predicted during the SEM images.

In 1.4452 the SFE at 20K is already very low (0.1 - 0.85 mJ/m^2). Thus, no significant decrease of the SFE in a hydrogen environment can be observed. Heavier loadings, while keeping the sliding speed constant, leads to higher plastic deformation and consequently a higher deformation rate on the microscale. The steep increase of twinning in the entire deformation process at high deformation energies accommodates deformation and internal stresses by higher strain rates at low temperature.

On the other hand in the high-alloyed steel 1.4876 with a high SFE, the decreasing hydrogen uptake with severe increases of loading leads to a marked SFE increase. Therefore, in case of weaker loading, twinning plays an important role in the deformation process and crack formation is observed. The low twin density after heavy loading corroborates this hypothesis about increased SFE and is responsible

for the low crack density at the worn surface. Hydrogen uptake in austenitic steels takes place by hydrogen pair formation within the faulted zone [PON97, HER98,JUA02]. Therefore, in alloys with high SFE, where the separation of the partial dislocations is very small and thus the faulted zones are very narrow, the hydrogen uptake may be hampered, especially if hydrogen release is favored by an intensified degradation of the surface zone at heavy loadings.

In case of the alloys with low SFE, such as 1.4452, 1.4439 and 1.4301, hydrogen can be easily absorbed due to the generation of numerous lattice imperfections at the worn surface and the formation of extended faults. Thus, numerous intersecting slip bands, glide-twin interactions as well as pile-ups at grain and phase boundaries within the nanostructured surface zone are able to initiate microcracks, specially if localized stress peaks build up by a hydrogen induced pressure. On the other hand in alloys with a high SFE a facilitated release of hydrogen takes place at high deformation energies. Hence twinning, formation of slip bands and cracking appear only at low deformation energies.

Texture formation during friction was analyzed using X-ray diffraction techniques. Preferred crystallite orientation, i.e. crystallographic texture, may arise during fabrication, manufacturing [HON84] and deformation of metals, such as during wear [HIR83,WHE75]. In all alloys investigated the observed trend was the same. The changes concerning the deformation mechanisms with temperature are directly reflected into the texture formation.

The (211)<111>-texture formed in the austenite after few cycles at RT is a rolling texture in fcc-materials at low deformation levels [WAS62]. With increasing number of cycles and after leaving the running-in regime the texture turns into a <111>-fiber texture along the scar normal direction. This kind of texture formation was often observed after sliding friction of fcc-metals [WHE75,ZUM87,FAR01]. Thus, the (111)-lattice planes, i.e. the slip planes of the fcc-lattice, are turned into an orientation nearly parallel to the scar plane. This way the lines of the friction force act on the slip planes and favor shear deformation along the sliding direction. Therefore, the amount of plastic deformation and microstructural deterioration at RT depend among other things on the texture formation within the contact zone. X-ray diffraction methods as

well as TEM-studies reveal additionally a preferential orientation of the <110>-direction along the sliding direction.

In case of steel 1.4301, a <210>/<221>- double fiber texture is formed in the martensite. Both crystallographic directions are 20° tilted with respect to the <110>-direction. Therefore, a <110>-fiber texture is approximately formed along the scar normal direction according to the orientation relationship between austenite and martensite ($(111)_\gamma//(011)_\alpha$) and induced by plastic deformation as well. Thus, the slip planes of the martensite are aligned nearly parallel to the scar surface and the shear deformation within the contact zone by the friction force is facilitated as in case of the austenite. In addition the texture formed in the martensite after 7700 cycles in air at RT does not differ significantly from the texture formed after 1200 cycles.

At cryogenic temperatures a (110)<111>-rolling texture is built up in the austenite as a result of increasing twinning in the deformation process. A similar texture formation was already observed in brass-alloys with low SFE after rolling with high deformation levels [WAS62,BUN93,HU66]. Hu proposed in his model [HU66], that with increasing deformation levels the twinning systems in CuZn-alloys are activated. As shown by microscopy and X-ray diffraction studies, twinning increases markedly during sliding friction of austenitic steels with decreasing temperature. Thus, the (112)<111>-initial texture starts gradually disappearing in favor of a (110)<112>-rolling texture.

The martensite is at cryogenic temperatures not plastically deformed and inherits consequently the preferential orientation formed in the austenite. Therefore, a <111>-fiber texture builds up along the scar normal direction according to the orientation relationship between austenite and martensite ($(111)_\gamma//(011)_\alpha$). Additional texture formation in the martensite during friction at cryogenic temperatures is visible during TEM-studies. A <110>-texture component appears along the sliding direction. This was often observed in bcc-materials after rolling [WAS62,BUN93].

The internal stress analysis revealed in all steels the formation of compressive stresses within the worn zone. During the deformation, when the counterbody is pressed against the steel surface, the steel contact zone is elongated and thus tensile stresses are introduced into the worn surface. When the shear strength is

reached, the metallic contact zone is plastically deformed. After deformation, the elastic part of the entire elongation is relieved and the wear scars remain under compressive stresses. Therefore, the compressive internal stresses within the wear grooves evaluated after friction indicate the magnitude of the tensile stresses, which act in the contact zone during the deformation.

The internal stresses in the steel 1.4301 depend on the scar direction and exhibit higher values along the scar radial direction. In the sliding direction material is continuously removed from the surface, whilst along the radial direction material is laterally compressed and plowing is observed. Hence the internal stresses along the sliding direction are relaxed due to an intense material removal from the surface and lower internal stress values are observed. In case of the stable alloy 1.4439 lower compressive stresses are built up in comparison to the steel 1.4301 and the stress state is rather independent from the scar direction. Higher compressive stresses in the alloy 1.4301 arise due the formation of martensite within the contact zone. Martensite exhibits a larger specific volume and induces additional compressive stresses into the austenite. The rotation symmetric stress state in the steel 1.4439 is likely due to the increased ductility of the austenite, which can easily undergo plastic deformation along all scar directions. In addition stress relaxation along the sliding direction is visible in the steel 1.4301 after friction in LH_2. This is due to the preferential crack formation along the radial scar direction observed during friction in LH_2.

With respect to the crack formation in LH_2, it could be shown that at 20 K the yield strength is very high and texture hardening occurs. In addition the compressive stress states after wear indicate the formation of high tensile stresses in the contact zone during friction. The reduced ductility combined with the mentioned defect interactions, pile-ups at the numerous grain and phase boundaries and the hydrogen induced pressure within the nanostructured surface zone results in local stress peaks, which are able to initiate microcracks.

7 Summary and Conclusions

In the present study the effect of temperature, environment and loading conditions on the wear and deformation behavior of austenitic stainless steels with different stacking fault energies (SFE´s) was studied during friction in cryogenic environments. Special attention was paid to cryogenic wear in hydrogen. Five German steel grades with distinct Ni-(Mn-) and N-contents were chosen for the investigations. They offered a continuous SFE variation for the metastable austenite. The other microstructural parameters, such as grain size and volume fraction of inclusions and δ-ferrite, which also affect the mechanical strength of austenitic steels, did not vary considerably for the different alloys investigated. As cryogenic environments/temperatures served liquefied gaseous mediums: nitrogen (LN_2, 77 K), hydrogen (LH_2, 20 K) and helium (LHe, 4.2 K). At room temperature (RT) the influence of the relative air humidity was additionally evaluated. All results reported here are published in [ASS03,ASS03I,ASS04,ASS04I,ASS04II,ASS04III,HÜB03,HÜB03I,HÜB04,PIN03,PIN03I,PIN04,PIN04I,PIN04II,PIN04III,PIN05,PYZ04].

The wear tests revealed that for the materials investigated the wear amount at RT and LN_2 is nearly the same. At RT humid air induces less wear. At these temperatures/environments the higher the stacking fault energy (SFE) the better the wear resistance is. However, an appreciable increase of hardness, such as in the N-high alloyed CrMn-steel 1.4452, leads similarly to a good wear performance in spite of a low SFE. At lower temperatures (LH_2 and LHe) wear decreases significantly and is similar for all steels, except for the alloy 1.4876, which is strongly affected by the presence of H_2. The study of the influence of the loading conditions on the wear performance in LH_2 showed that at mild tribological stressing (F_N = 5 N, v = 0.06 m/s) the wear resistance of all materials investigated is basically the same. Increasing sliding speeds (v = 0.2 m/s) reduced the wear in all N-alloyed steels, whereas for the N-free steel 1.4876 a linear increase was observed. At more severe loadings (F_N = 10 N, v = 0.2 m/s) the chemical composition and consequently the SFE determine the wear performance. Low SFE´s lead clearly to a better wear resistance.

Sliding friction in inert environments, such as air, LN_2 and LHe, does not induce crack formation within the contact zone. On the contrary extensive crack networks are

formed during friction in LH_2. However, the hydrogen-induced embrittlement is not necessarily correlated to a reduced wear performance. Low SFE materials with good wear resistance exhibit a more intense crack formation. Furthermore the cracking process is affected by the tribological stress conditions. For high SFE alloys an increase of loading suppresses crack formation due to a facilitated hydrogen release.

High SFE´s inhibit strain-induced martensite formation down to 4.2 K in LHe. CrNi steels with low SFE undergo a direct $\gamma \rightarrow \alpha$' transformation already at RT, whilst CrMn steels are stable at RT and ε-martensite formation occurs only at cryogenic temperatures and heavy loadings. The amount of martensite present at the worn surface depends strongly on the number of loading cycles due to fragment spallation of the brittle martensitic layers. In FeCrNi-alloys with low SFE the martensite content generated in the wear scar depends strongly on temperature. A maximum volume fraction is encountered about 77 K in LN_2. With further cooling down to 20K in LH_2 the strain-induced phase transformation is hampered and lower martensite contents are observed. Tribological stress conditions and environment influence the martensite formation as well. In sliding friction increased normal forces lead to more intense martensite formation, whereas changes in the sliding velocity only have a minor influence on plastic deformation and martensitic transformation. In humid air thinner oxide layers are formed and plastic deformation along with martensite formation in the substrate are reduced.

Plastic deformation in austenitic steels at RT is chiefly due to dislocation slip. In case of low SFE twinning is also activated in a minor extent. With decreasing temperatures the SFE decreases linearly with temperature, planar dislocation arrangements take place and the role of twinning in the plastic deformation process increases. Twinning dominates the plastic deformation during friction in LH_2, 20 K and in LHe, 4.2 K. In LH_2 hydrogen is adsorbed by the contact zone and the loading conditions are locally increased. Furthermore the adsorbed hydrogen brings about an additional decrease of SFE and increase of twinning. Increased local stresses along with texture hardening, low dislocation density and numerous interactions between the new generated lattice imperfections match the requirements for crack initiation and propagation during friction in LH_2. For high SFE steels the crack formation in the

contact zone after wear in LH_2 depends on the loading conditions and is related to the ease of keeping hydrogen soluted in the austenite lattice.

Regarding applications in cryogenic tribosystems it can be derived that the chemical composition of austenitic steels determines the wear resistance at cryogenic temperatures. Moderate N-additions enhance the stability of the austenitic microstructure and the wear performance at cryogenic temperatures. High N-contents, particularly in CrMn steels, induce a ductile to brittle transition in the top surface layer at extremely low temperatures, but the increased hardness determines a better wear resistance. In general low SFE matches the requirements for a good wear performance. Extreme low SFE´s are connected to a loss of toughness at cryogenic temperatures, but the wear resistance seems to be not affected. The performance during tribological loading of austenitic alloys with high SFE can be clearly improved by small N-additions. High Ni-contents as well as its replacement by Mn in austenitic steels avoid the formation of the strain induced α-martensite. However, it could be shown that strain induced α-martensite does not cause a loss of wear resistance at cryogenic temperatures and should be avoided only in case of applications in the superconductivity. In CrMn steels a γ/ε-phase transformation is possible with increasing loadings, but the wear performance remains also the same.

8 Recommendations for Practical Use

For practical purposes it follows that:

- For tribological applications at RT: the steels 1.4591 and 1.4452 are recommended for sliding friction, whereas for fretting all investigated steel grades exhibit similar performances;
- For tribological applications at cryogenic temperatures: the steels 1.4452 and 1.4591 are recommended, whereas all other steel grades investigated exhibit an intermediate performance;
- For tribological applications in LH_2: the steels 1.4301 and 1.4452 are recommended and the steel 1.4876 should be avoided;
- For applications in the superconductivity: The steels 1.4439 and 1.4452 are recommended and the steel 1.4301 should be avoided.

Tab.2 gives an overview about the applicability of each steel investigated.

9 References

[AHN79] T. M. Ahn, P. J. Blau, K. L. Hsu, D. A. Rigney, J. D. Schell, *Wear*, 56, 1979, 409-413

[ASS03] K. Aßmus, W. Hübner, J. Bohse, H. Pinto, A. Pyzalla, *14. Kolloquium Schallemission*. *DGZfP-Berichtsband 82*, ISBN 3-931381-41-2, Berlin-Adlershof, 27-28 March, 2003, 89-102

[ASS03I] K. Aßmus, W. Hübner, A. Pyzalla, H. Pinto, *Proc. 44.Tribologie-Fachtagung 2003*, Bd. I, Göttingen, 22-24 September, 2003, 6/1-6/8

[ASS04] K. Assmus, W. Hübner, A. Pyzalla, H. Pinto, *Proc. 14th International Colloquium Tribology*, vol. II, ISBN 3-924813-54-X, Ostfildern, 13-15 January, 2004, 1047-1054

[ASS04I] K. Aßmus, S. Binkowski, W. Hübner, D. Klaffke, S. Benemann, A. Pyzalla, H. Pinto, *Fortschritte in der Metallographie. Sonderbände der Praktischen Metallographie*, 35, 2004, 207-212

[ASS04II] K. Aßmus, W. Hübner, A. Pyzalla, H. Pinto, *Tribologie und Schmierungstechnik*, 51, 3, 2004, 30-33

[ASS04III] K. Aßmus, W. Hübner, A. Pyzalla, H. Pinto, *Tribotest Journal*, in press

[BER00] Berliner Zeitung, 12.05.2000

[BER00I] W. Bergmann, *Werkstofftechnik*, ISBN 3-446-21409-7, Carl Hanser Verlag, Munich, 2000

[BUN93] J. Bunge, E. Dahlem-Klein, H. Klein, N. J. Park, *Program System ODF – Analysis*, Cuvillier Verlag, Göttingen, Germany, 1993

[BUN93I] H.-J. Bunge, P. R. Morris, *Texture Analysis in Materials Science*, Cuvillier Verlag, 1993, Göttingen

[BUT73] E. D. Butakova, *Fizika Met. Metalloved.*, 35, 1973, 662

[CHA00] A. Chanda, M. De, *J. Alloys Comp.*, 313, 2000, 104

[CHR95] J. W. Christian, S. Mahajan, *Prog. in Mat. Sci.*, 39, 1995, 1-157

[DEI01] P. Deimel, H. Fischer, *Proc. MAT2001 Int. Conf. Material Testing and Research*, Nürnberg, 8-10.05.2001, 135-139

[DIA98] J. M. Diani, D. M. Parks, *J. Mech. Phys. Solids*, 46, 9, 1998, 1613-1635

[DWV00] DWV Projektführer Wasserstoff, Deutscher Wasserstoff-Verband, Berlin, 2000

[ENZ88] S. Enzo, G. Fagherazzi, A. Benedetti, S. Polizzi, *J. Appl. Cryst.*, 21,

1988, 536

[FAN72] G. Faninger, U. Hartmann, *HTM*, 27, 1972, 233-244

[FAR01] Z. N. Farhat, *Wear*, 250, 2001, 401-408

[FEL89] H. G. Feller, B. Gao, *Wear*, 132, 1989, 1-7

[FIT03] M. E. Fitzpatrick, A. Lodini, *Analysis of Residual Stress by Diffraction using Neutron and Synchrotron Radiation*, Taylor & Francis, London, 2003

[FRE03] J. Freudenberger, A. Gaganov, A. L. Hickman, H. Jones, *Cryogenics*, 43, 2003, 133-136

[FRI01] K. Friedrich, W. Hübner, Tagungsband, BAM-Sonderheft 3, 2001

[GAV98] V. G. Gavriljuk, A. L. Sozinov, J. Foct, J. N. Petrov, Y. A. Polushkin, *Acta mater.*, 46(4), 1998, 1157-1163

[GAV99] V. G. Gavriljuk, H. Berns, *High Nitrogen Steels*, ISBN 3-540-66411-4, Springer Verlag, Berlin, 1999, 169-173

[GRA01] T. Gradt, H. Börner, Th. Schneider, *Tribology Intern.*, 34, 4, 2001, 225-230

[GRA01l] T. Gradt, H. Börner, W. Hübner, Ye. Ostrovskaya, *Proc. 3rd European Conf. On Launcher Technology*, ,,Structures and Technologies, Challenges for Future Launchers'', 11-14.12.2001, Strasbourg, 927-935

[GRO90] J. Grosch, *Schadenskunde im Maschinenbau*, ISBN 3-8169-1761-5, Expert Verlag, Renningen-Malmsheim, 1990, 295

[HAR90] M. A. E. Harzenmoser, Doctoral thesis, Eidgenössische Technische Hochschule, Zürich, 1990

[HAU97] V. Hauk, *Structural and Residual Stress Analysis by Nondestructive Methods*, Elsevier, Amsterdam, 1997

[HEL96] K. Helmig, Habilitation thesis, TU Clausthal, 1996

[HER98] J. D. Hermida, A. Roviglione, *Scr. Mat.*, 39(8), 1998, 1145-1149

[HIR83] J.P. Hirth, D.A. Rigney, In: F.R. Nabarro (Ed.), *Dislocations in Solids*, Vol. 6, North-Holland, Amsterdam, 1983, 10

[HOL68] M. L. Holzworth, M. R. Louthan jr., *Corrosion*, 24(4), 1968, 110-124

[HON84] R. W. K. Honeycomb, *The Plastic Deformation of Metals*, 2nd Edition, Edward Arnold Ltd., UK, 1984, 326

[HSU80] K.-L. Hsu, T. M. Ahn, D. A. Rigney, *Wear*, 60, 1980, 13-37

[HU66] H. Hu, R. S. Cline, S. R. Goodmann, *Recrystallization Grain Growth and*

Texture, ASM, 1966, Metals Park, Ohio

[HÜB02] W. Hübner, D. Klaffke, *Proc. Tribologie-Fachtagung 2002*, Göttingen, Germany, 1, Sept. 2002, 10/1-10/11

[HÜB03] W. Hübner, T. Gradt, K. Assmus, A. Pyzalla, H. Pinto, S. Stuke, *Proc. Hydrogen and Fuel Cells 2003. Conference and Trade Show*, Vancouver, Canada, 8-11 June, 2003

[HÜB03I] W. Hübner, K. Aßmus, A. Pyzalla, H. Pinto, *Proc. HYPOTHESIS V. Hydrogen Power Theoretical and Engineering Solutions Int. Symp.*, ISBN 88-86281-90-0, Porto Conte, Italy, 7-10 September, Padova: Servizi Grafici Editoriali, 2003, 581-588

[HÜB04] W. Hübner, H. Assmus, A. Pyzalla, H. Pinto, *Fortschritte in der Metallographie*. *Sonderbände der Praktischen Metallographie*, 35, 2004, 399-404

[HYF00] Hyforum 2000, The International Hydrogen Energy Forum 2000, Policy – business –Technology, *Proc. Vol. I + II*, EFO Energy Forum GmbH, Bonn, 2000

[KOH99] Y. Kohno, H. Konishi, K. Shibata, K. Watanabe, S. Awaji, *Mat. Sci. Eng. A 273-275*, 1999, 333-336

[JON88] H. Jones, F. Herlach, J. A. Lee, H. M. Whitworth, A. G. Day, D. J. Jeffrey et al., *Proc. of 10th International Conf. On Magnet Technology (MT-10)*, Boston, IEEE Trans Magn, 24, 1988, 1055

[JON97] H. Jones, M. Van Cleemput, In: Schneider-Muntau HJ, editor. *High Magnetic Fields*. Singapore: World Scientific, ISBN 9810231253, 1997

[JUA02] A. Juan, L. Moro, G. Brizuela, E. Pronsato, *Int. J. Of Hydrogen Energy*, 27, 2002, 333-338

[LAN71] R. M. Lantaniason, A. W. Ruff, *Metall. Trans.*, 2, 505, 1971

[LEB00] A. Le Bail, *Proc. of 6th International School and Workshop of Crystallography*, 22-27 January, 2000, Ismailia, Egypt

[LIN01] M. Linder, N. Rando, A. Peacock, B. Collandin, *ESA BULLETIN*, 107, Aug. 2001, 92-105

[LIU98] S. C. Liu, T. Hashida, H. Takahashi, H. Kuwano, Y. Hamaguchi, *Metall. Mat. Trans.*, 29A, 3, 1998, 791-798

[LUT90] L. Lutterotti, P. Scardi, P. Maistrelli, *J. Appl. Cryst.*, 23, 1990, 246-252

[LUT98] L. Lutterotti, S. Gialanella, *Acta Materialia*, 46[1], 1998, 101-110

[MAC61] E. Macherauch, P. Müller, *Z. f. angew. Phy.*, 13, 1961,305-313

[MCH83] H. I. Mc Henry, In: R. P. Reed, T. Horiuchi, editors. *Austenitic steels at low temperatures*. New York and London: Plenum Press, 1983

[MÜL94] P. Müllner, C. Sollenthaler, P. J. Uggowitzer, M. O. Speidel, *Acta Materialia*, 42, 7, 1994, 2211-2217

[MÜL97] P. Müllner, *Mat. Sci. Eng. A*, 234-236, 1997, 94-97

[NOH77] K. Nohara, Y. Ono, N. Ohashi, *J. Iron Steel Inst. Jpn.*, 63, 1977, 212-222

[NOY87] I. C. Noyan, J. B. Cohen, *Residual Stress : Measurement by Diffraction and Interpretation*, Springer-Verlag, New York, 1987

[NYI93] A. Nyilas, B. Obst, H. Nakajima, *Proc. 3rd Int. Conf. High Nitrogen Steels-93*, Kiev, Sept. 1993, 139

[NYI93I] A. Nyilas, B. Obst, H. Nakajima, In : V. G. Gavriljuk and V.M. Nadutov (eds). *High Nitrogen Steels*, HNS 93, Institute for Metal Physics, Kiev, 1993, 339-344

[OBS91] B. Obst, A. Nyilas, *Mat. Sci. Eng. A*, 137, 1991, 141-150

[OH99] H.-K. Oh, K.-H. Yeon, H. Y. Kim, *J. Mater. Process. Technol.*, 95, 1999, 10-16

[OST01] Ye. L. Ostrovskaya, T. P. Yukhno, G. D. Gamulya, Yu. V. Vvedenskij, V. I. Kuleba, *Tribology Intern.*, 34, 2001, 4, 267-278

[PEP92] W. Pepperhoff, In: Verein Deutscher Eisenhüttenleute (Ed.) Steel Vol. 1, *Physical Properties*, Springer Verlag, Berlin, 1992, 397-402

[PIN03] H. Pinto, S. Stuke, A. Pyzalla, W. Hübner, K. Aßmus, *Proc. Tribologie-Fachtagung 2003*, Göttingen, 22-24 September, 2003, Bd. I, 7/1-7/10

[PIN03I] H. Pinto, A. R. Pyzalla, W. Hübner, K. Aßmus, S. Stuke, HASYLAB Annual report, 2003

[PIN04] H. Pinto, *Verformungsmechanismen und Eigenspannungen nach Verschleiß von 1.4301 und 1.4439 in tiefkalten Medien*, oral presentation, Sitzung des Fachausschusses Eigenspannungen der AWT, 6-7 November, Hause Daimler Chrysler, Stuttgart, 2003

[PIN04I] H. Pinto, A. Pyzalla, W. Hübner, K. Aßmus, *Influence of Environment, Temperature and Chemical Composition on the Microstructural Deterioration of CrNi Steels during Friction*, oral presentation, Reibung und Verschleiß, DGM-Tagung, 10-12 March, Fürth, 2004

[PIN04II] H. Pinto, A. Pyzalla, W. Hübner, K. Aßmus, *Materialwissenschaft und*

Werkstofftechnik, 35, 10-11, 2004, 716-721

[PIN04III] H. Pinto, A. R. Pyzalla, W. Hübner, K. Aßmus, HASYLAB Annual report, 2004

[PIN05] H. Pinto, A. Pyzalla, R. Büscher, A. Fischer, K. Aßmus, W. Hübner, *Wear*, 2005, in press

[POP98] N. C. Popa, *J. Appl. Cryst.*, 31, 1998, 176-180

[PYZ04] A. Pyzalla et al. (H. Pinto, T. Poeste, C. Bohne, W. Reimers, K. Assmus, W. Hübner, A. Fischer), *Proc. 14th International Colloquium Tribology*, Vol. I, ISBN 3-924813-54-X, Ostfildern, 13-15 January, 2004, 85-89

[REM77] L. Remmy, A. Pineau, *Mat.Sci. Eng.*, 28, 99, 1977

[RHO77] C. G. Rhodes, A. W. Thompson, *Metall. Trans. 8A*, 1977, 1901

[ROB01] L. M. Robertson, *Eng. Fracture Mech.*, 68, 2001, 671-692

[RIG77] D. A. Rigney, W. A. Glaeser, *Wear of Materials 1977*, American Society of Mechanical Engineers, New York, 1977, 41-45

[SAH02] P. Sahu, M. De, S. Kajiwara, *Mat. Sci. Eng. A*, 333, 2002,10-23

[SAH02I] P. Sahu, M. De, S. Kajiwara, *J. Alloys Comp.*, 346, 2002, 158-169

[SCA94] P. Scardi, L. Lutterotti, P. Maistrelli, *Powder Diffraction*, 9(3), 1994, 180-186

[SCH75] R. E. Schramm, R. P. Reed, *Metall. Trans. A*, 6A, 1975, 1345-1351

[SCH75I] H. Schumann, *Kristall u. Technik*, 10, 1975, 401-411

[SCH91] H. Schumann, *Metallographie*, ISBN 3-342-00431-2, Deutscher Verlag für Grundstoff Industrie, Stuttgart, 1991

[SCH98] W. Schatt, E. Simmchen, G. Zouhar, *Kronstruktionswerkstoffe des Maschinen- und Anlagenbaues*, Deutscher Verlag für Grundstoffindustrie, Stuttgart, 1998

[SEE55] A. Seeger, *Phil. Mag.*, 46, 1955, 1194

[SPI98] E. Spinadel, F. Gamallo, S. L. Garcia Nunez, P. Spinadel, M. Cervino, *Proc. 12thWorld Hydrogen Energy Conf.*, Buenos Aires, June 1998, 1, 369

[STA01] Stahlschlüssel Taschenbuch, ISBN 3-922 599-16-8, Verlag Stahlschlüssel Wegst GmbH, Marbach, 2001

[TAO02] N. R. Tao, Z. B. Wang,W. P. Tong, M. L. Sui, J. Lu, K. Lu, *Acta materialia*, 50, 2002, 4603-4616

[THE02] G. Theiler, W. Hübner, T. Gradt, P. Klein, K. Friedrich, *Tribology Intern.*, 35, 7, 2002, 449-458

[TOB88] R. L. Tobler, D. Meyn, *Metall. Trans.*, 19A, 6, 1988, 1626-1631

[TOM90] Y. Tomota, S. Endo, *ISIJ Intern.*, 30, 8, 1990, 656-662

[TOM98] Y. Tomota, J. Nakano, Y. Xia, K. Inoue, *Acta Materialia*, 46, 9, 1998, 3099-3108

[TOM98I] Y. Tomota, Y. Xia, K. Inoue, *Acta Materialia*, 46, 5, 1998, 1577-1587

[WAR69] B. E. Warren, *X-Ray Diffraction*, Addison-Wesley, Reading, MA, 1969, Chapter 13

[WAS62] G. Wassermann, J. Grewen, *Texturen metallischer Werkstoffe*, Springer Verlag, 1962, Göttingen

[WER83] J. J. Wert, S. A. Singerman, S. G. Caldwell, D. K. Chaudhuri, *Wear*, 92, 1983, 213-229

[WER85] Werkstoffkunde Stahl, Bd. 2, Springer, Berlin, 1985, 285

[WHE75] D.R. Wheeler, D.H. Buckley, Wear, 33, 1975, 65

[WOL72] U. Wolfstieg, *HTM*, 27, 1972, 245-251

[WU02] X. Wu, N. Tao, Y. Hong, B. Xu, J. Lu, K. Lu, *Acta materialia*, 50, 2002, 2075-2084

[YOU93] R. A. Young, In: R. A. Young, editor. *The Rietveld Method*, Oxford University Press, 1993, Chapter 1

[ZAP47] C. Zapffe, *Amer. Soc. for Metals*, 39, 1947, 191-192

[ZHA03] H. W. Zhang, Z. K. Hei, G. Liu, J. Lu, K. Lu, *Acta materialia*, 51, 2003, 1871-1881

[ZUM87] K. Zum-Gahr, *Microstructure and wear of materials*, Elsevier, Amsterdam, 1987

10 Tables and Figures

Tab.1: Chemical composition of the investigated materials

Material*	SFE_{RT} [mJ/m^2]	Cr	Ni	Mn	Mo	C	N	Fe
1.4452	12	16,0-20,0	-	12,0-16,0	2,5-4,2	<0,15	0,75-1,0	bal.
1.4301	21	17,0-19,5	8,0-10,5	2,0	-	<0,07	<0,11	bal.
1.4439	30	16,5-18,5	12,5-14,5	1,5	4,0-4,5	0,03	0,12-0,22	bal.
1.4876	42	20,5	30,65	0,69	-	0,061	-	bal.
1.4591	71	32,85	30,95	-	1,67	0,007	0,39	bal.

* German steel grades

Tab.2: Applicability of the steel grades investigated

Material*	Tribosystems at RT		Cryogenic Tribosystems	Tribosystems in LH_2	Superconductivity
	Sliding	Fretting			
1.4301	↑	↑↑↑	↑↑	↑↑↑	↑
1.4439	↑	↑↑↑	↑↑	↑↑	↑↑↑
1.4876	↑↑	↑↑↑	↑↑	↑	↑↑
1.4591	↑↑↑	↑↑↑	↑↑↑	↑↑	↑↑
1.4452	↑↑↑	---	↑↑↑	↑↑↑	↑↑↑

* German steel grades

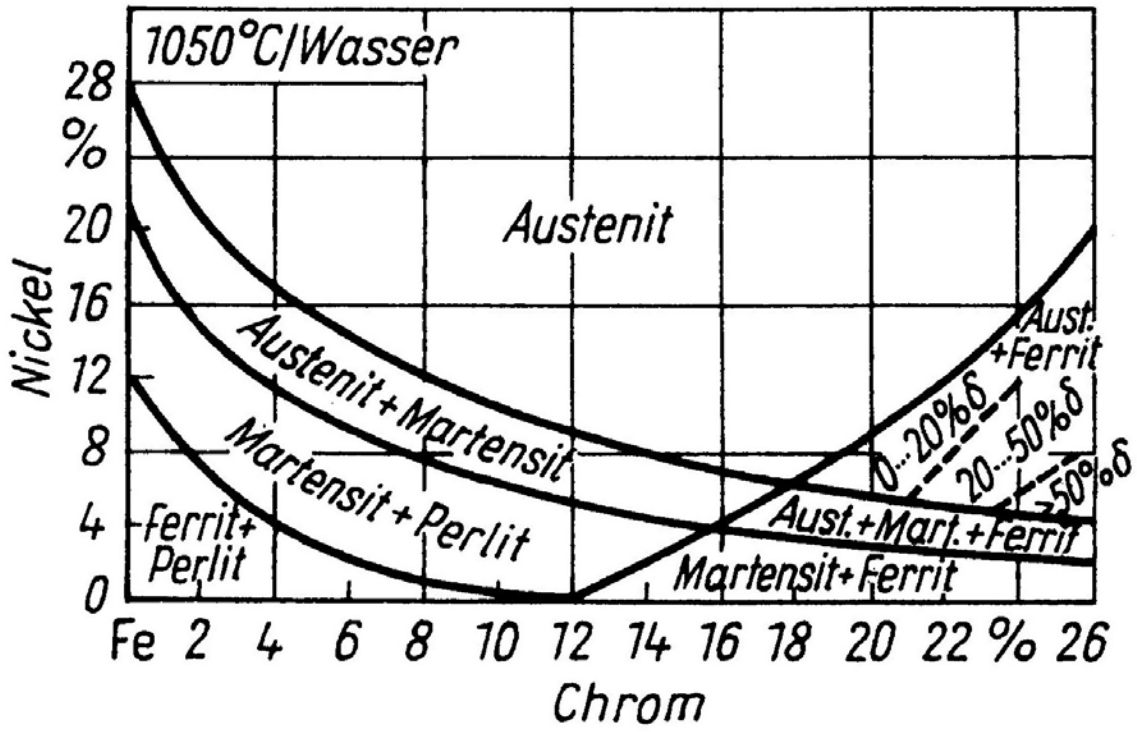

Fig.1: Maurer-Diagram showing microstructure formation in the CrNi-steels [SCH91]

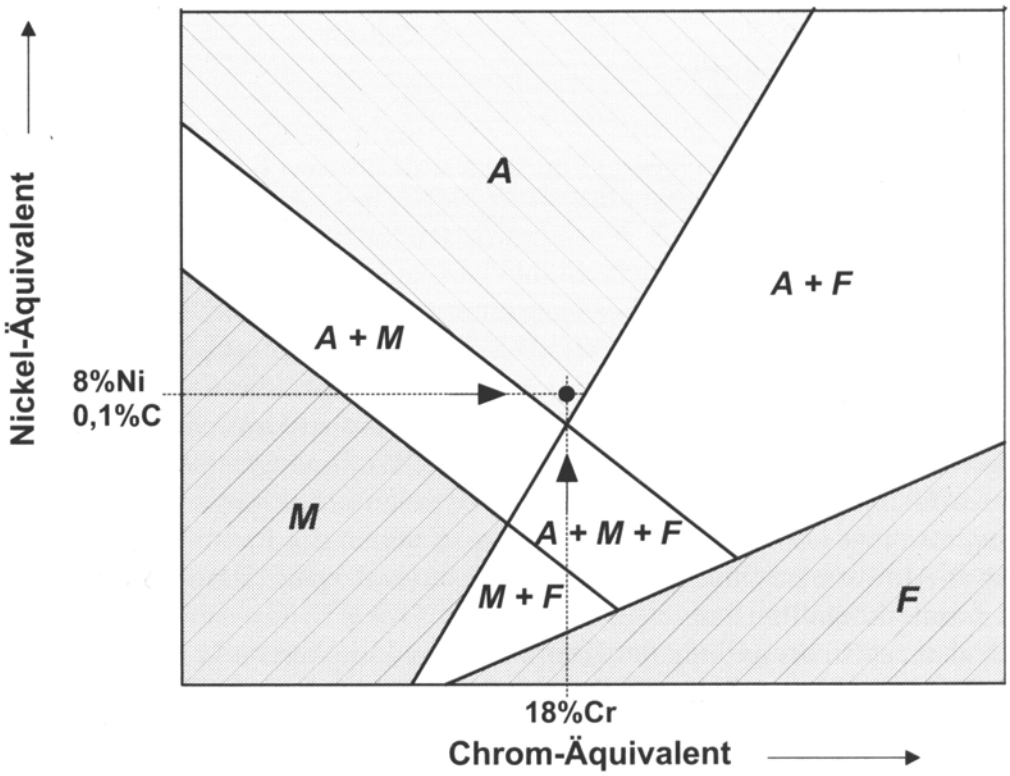

Fig.2: Schaeffler diagram for high alloyed CrNi-steels [BER00]

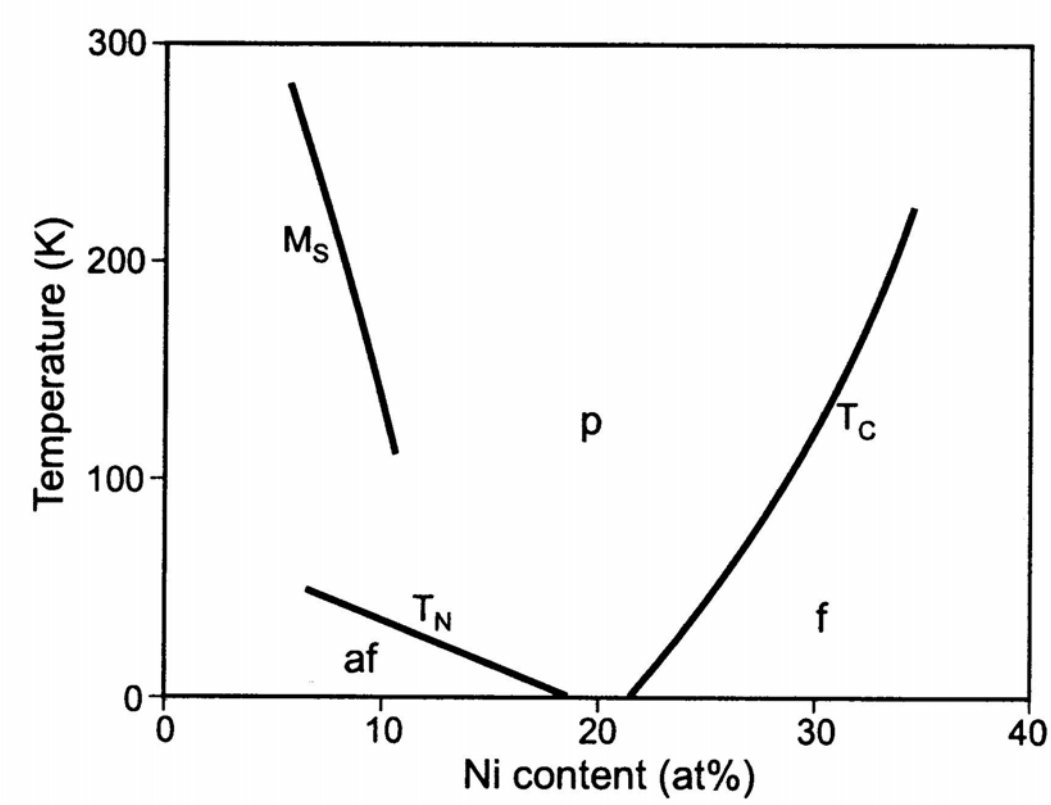

Fig.3: Magnetic transformation of paramagnetic (p) to antiferromagnetic (af) or ferromagnetic (f) austenite of a steel with 20 at% Cr and an increasing Ni-content [PEP92]

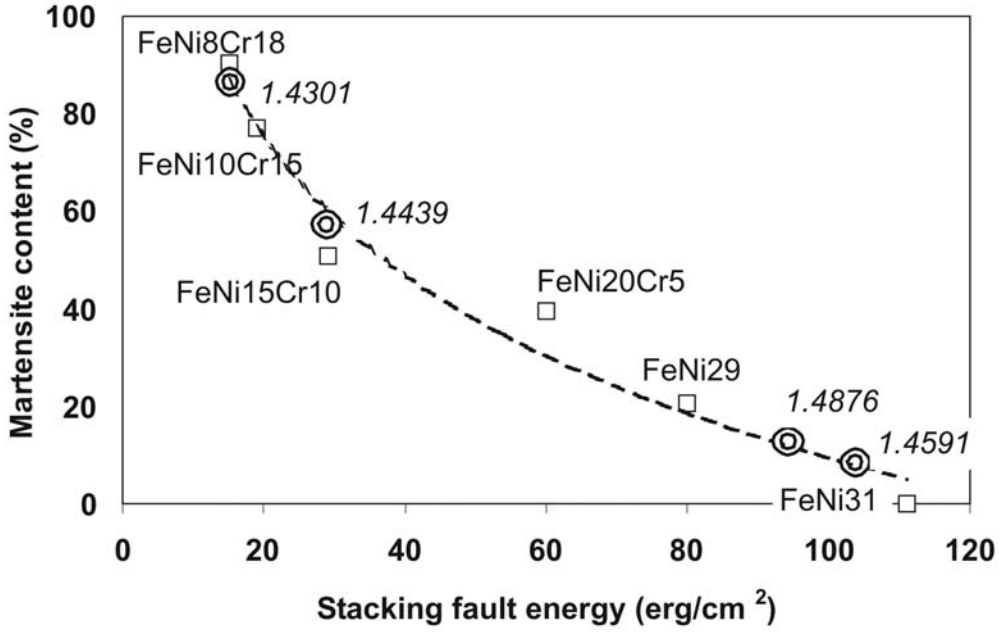

Fig. 4: Influence of the SFE of austenitic FeNiCr alloys on the martensite generation ([BUT73] modified)

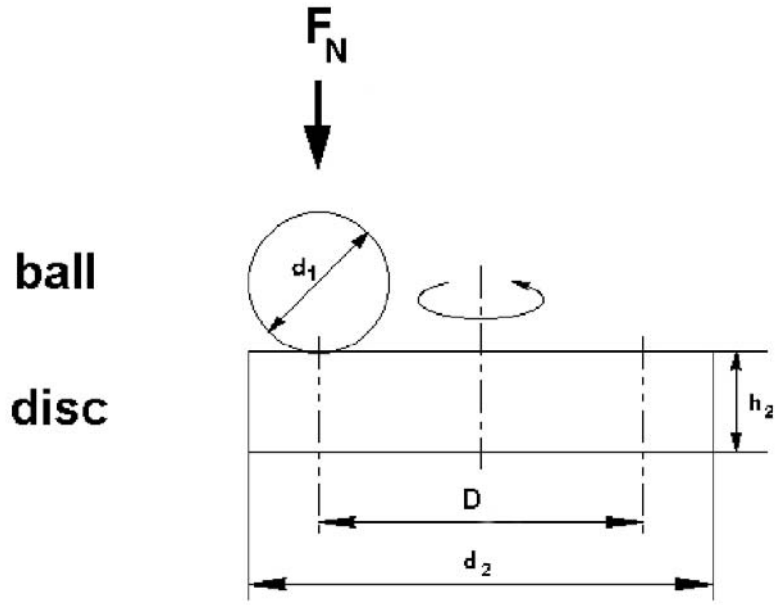

Fig. 5: Scheme of the ball-on-flat assembly used for sliding friction experiments in the cryotribometers (D - diameter of the circular wear track; d_1, d_2 – diameters of the ball and the disc resp.; h_2 – thickness of the disc)

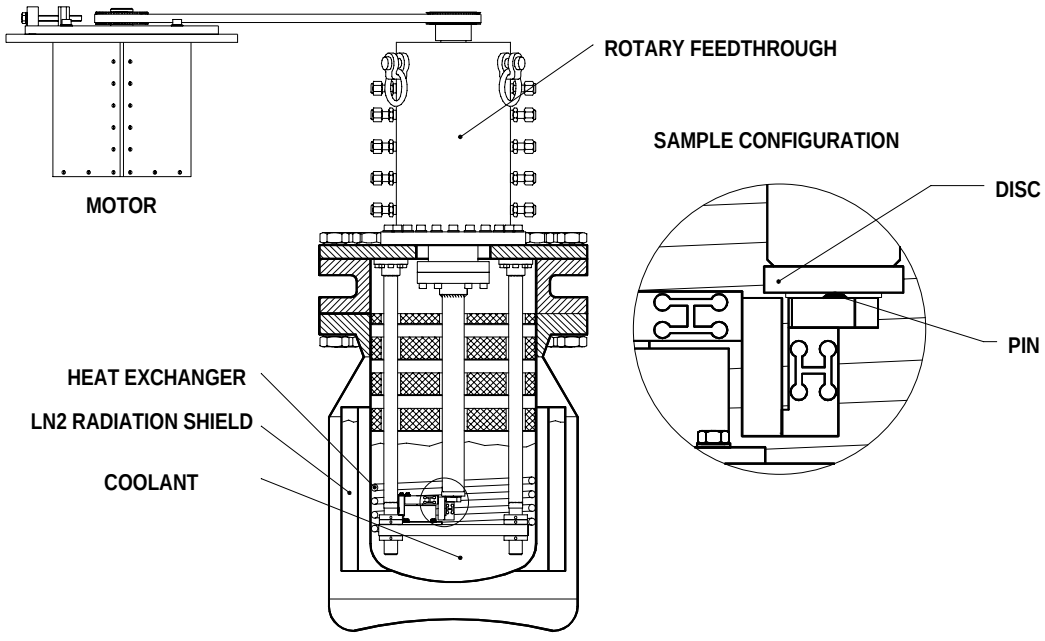

Fig. 6: Low-temperature tribometer CT3. Schematic drawing

Fig.7: Fretting-tribometer TKRD

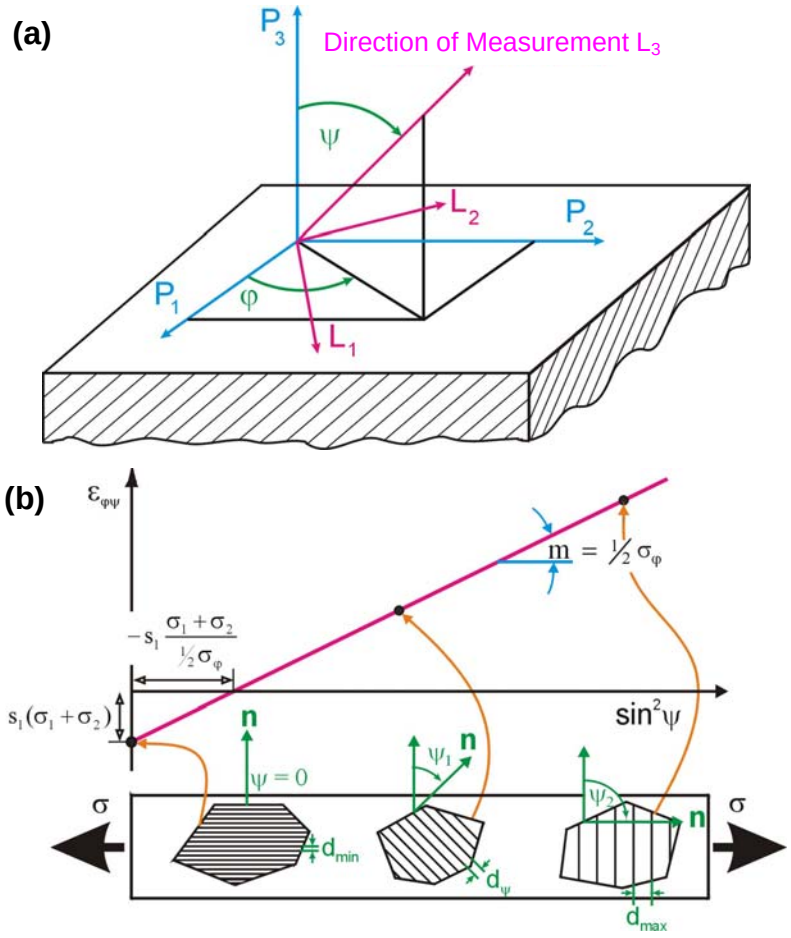

Fig.8: (a) Sample and laboratory coordination system, (b) Distribution of strains according to the $\sin^2\psi$-method

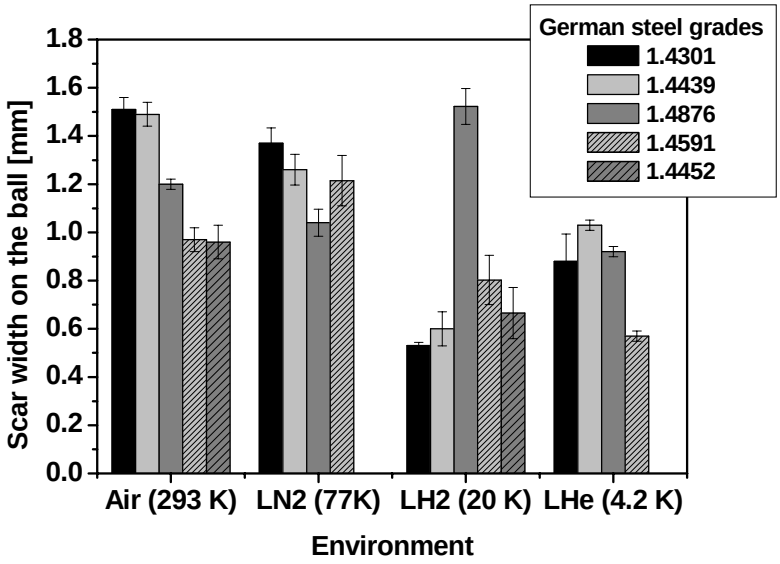

Fig.9: Effect of temperature (environment) on the wear resistance (F_N = 5 N, v = 0.2 m/s)

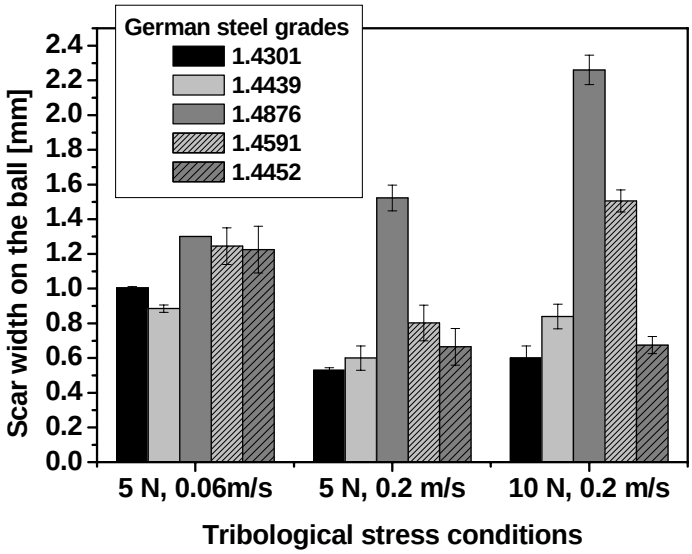

Fig.10: Effect of increasing sliding velocities and normal forces on the wear resistance

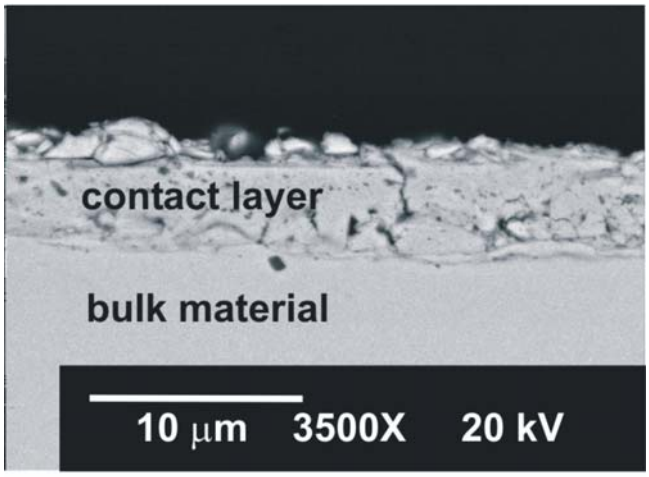

Fig.11: Tribologically modified zone in the steel 1.4301 after Friction in LH_2 (F_N = 5N, v = 0.06 m/s)

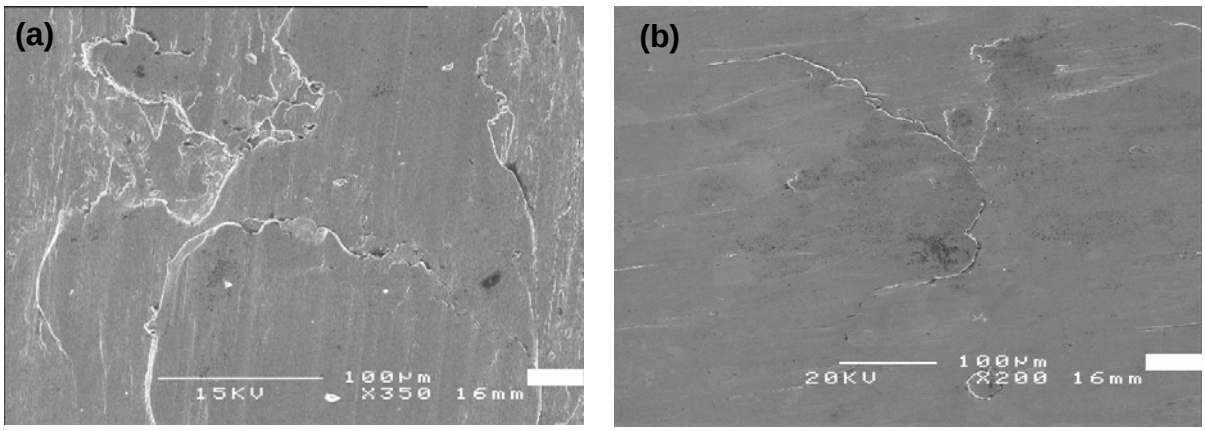

Fig.12: Wear scars after friction in LHe (F_N = 5N, v = 0.2 m/s)
(a) steel 1.4301, (b) steel 1.4439

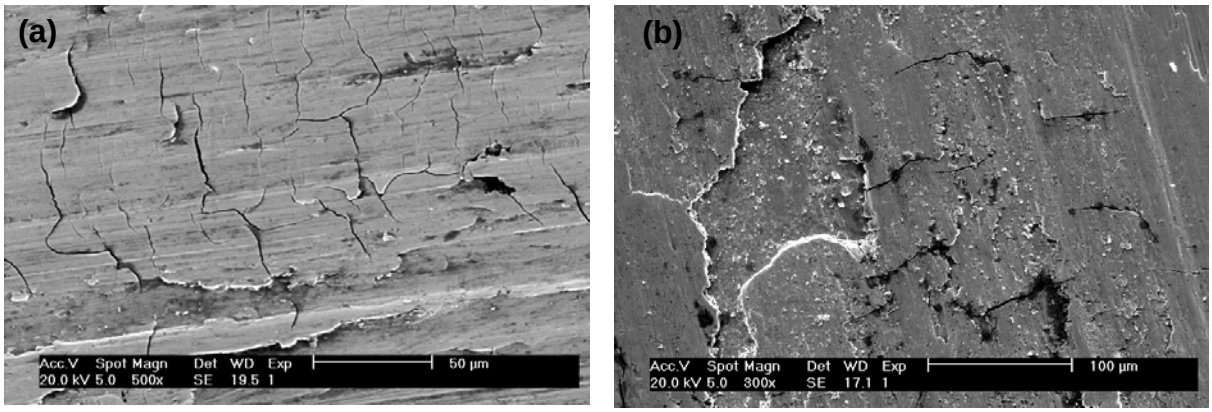

Fig.13: Typical crack pattern within the wear scars after friction in LH_2 (F_N = 5N, v = 0.06 m/s)
(a) steel 1.4439, (b) steel 1.4591

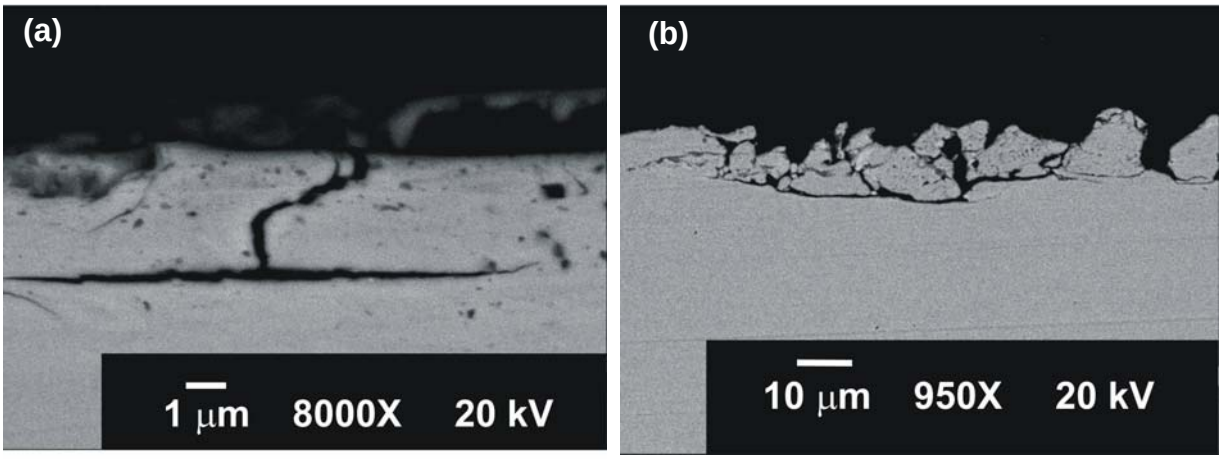

Fig.14: (a), (b) Crack propagation within the deformed contact layer in the steel 1.4301 after friction in LH_2 (F_N = 5N, v = 0.06 m/s)

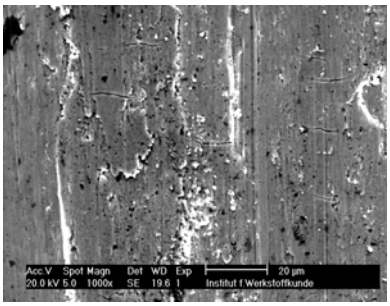

F_N = 5 N, v = 0.06 m/s

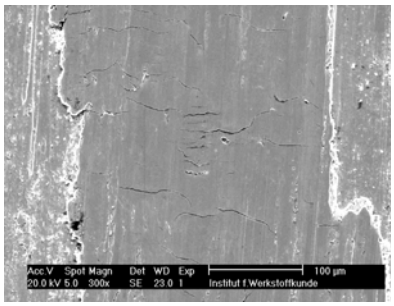

F_N = 5 N, v = 0.2 m/s

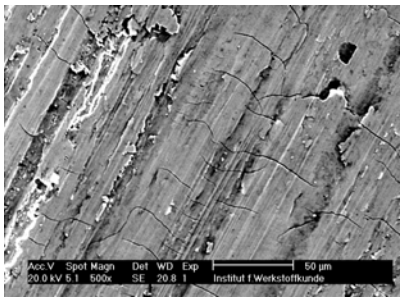

F_N = 10 N, v = 0.2 m/s

Fig.15: Steel 1.4452 after sliding friction in LH_2 at different loading conditions

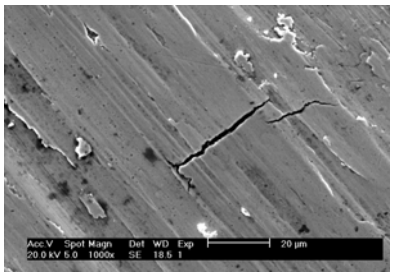

F_N = 5 N, v = 0.06 m/s

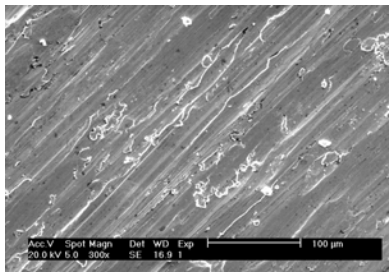

F_N = 5 N, v = 0.2 m/s

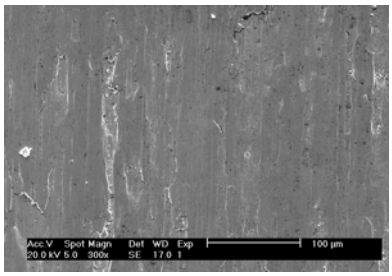

F_N = 10 N, v = 0.2 m/s

Fig.16: Steel 1.4876 after sliding friction in LH_2 at different loading conditions

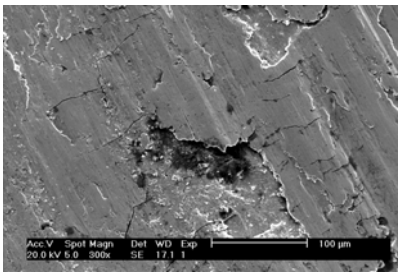

F_N = 5 N, v = 0.06 m/s

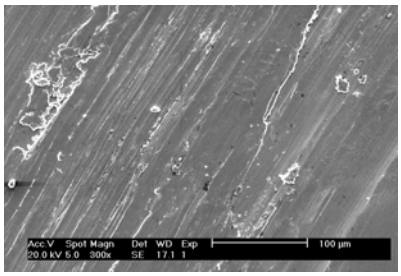

F_N = 5 N, v = 0.2 m/s

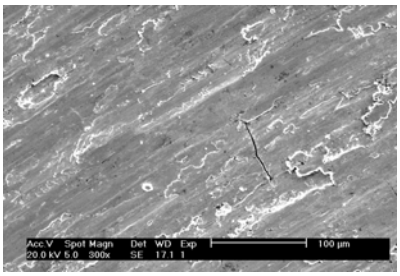

F_N = 10 N, v = 0.2 m/s

Fig.17: Steel 1.4591 after sliding friction in LH_2 at different loading conditions

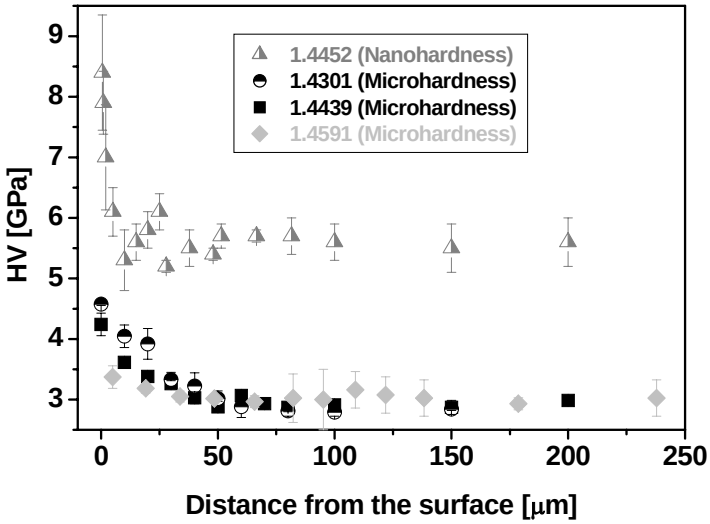

Fig.18: Hardness depth profiles of the near surface zones after friction in LH_2 with F_N = 5N and v = 0.06 m/s

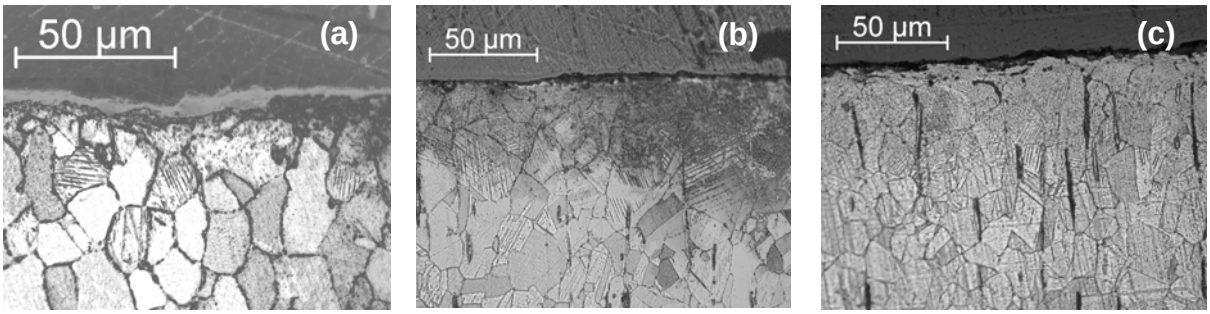

Fig.19: Microstructure of near surface zone in the steel 1.4301
(a) Air, (b) LN_2, (c) LH_2

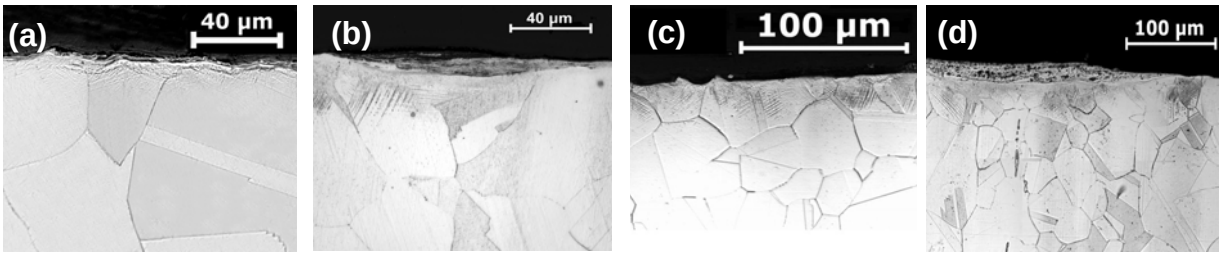

Fig.20: Microstructure of near surface zone in the steel 1.4439
(a) Air, (b) LN_2, (c) LH_2, (d) LHe

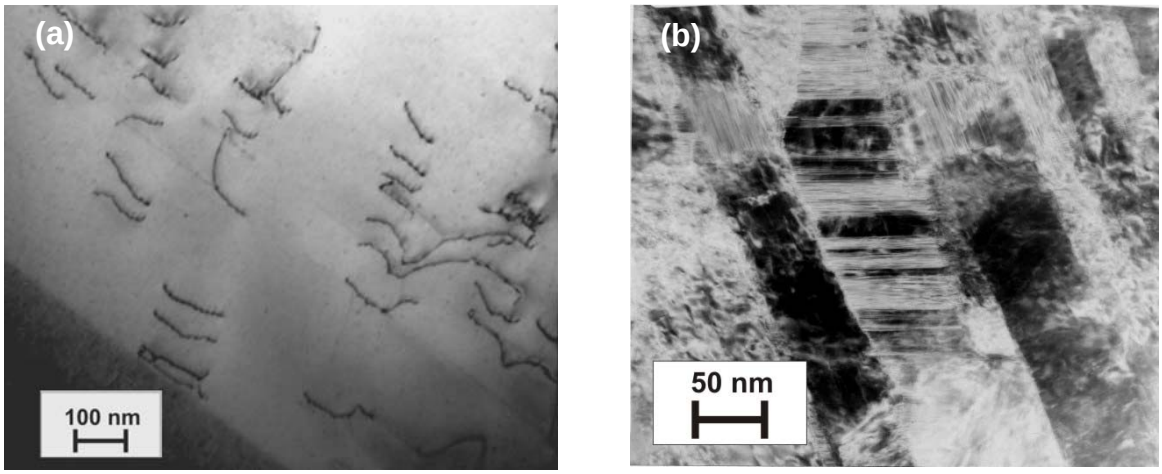

Fig.21: (a) Dislocation slip in the steel 1.4439 after friction at RT in air (F_N = 5N, v = 0.06 m/s), (b) Heavily twinned zone in the steel 1.4301 after friction in LH_2 (F_N = 5N, v = 0.06 m/s)

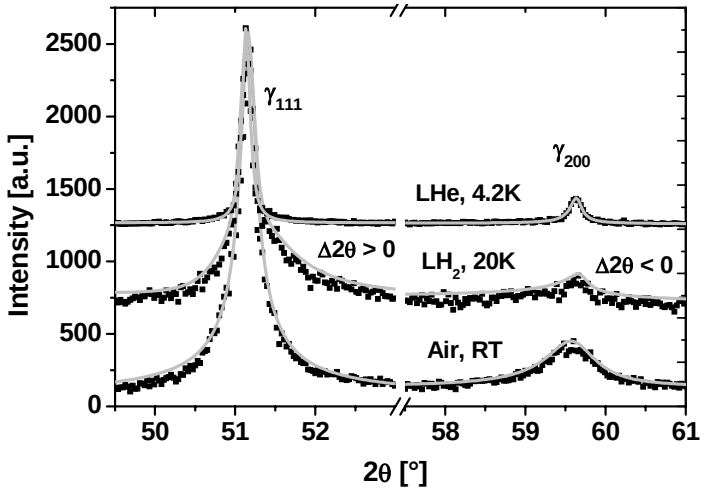

Fig.22: Synchrotron X-ray diffraction profile from the wear scars in the steel 1.4439 after friction in different environments (F_N = 5N, v = 0.06 m/s)

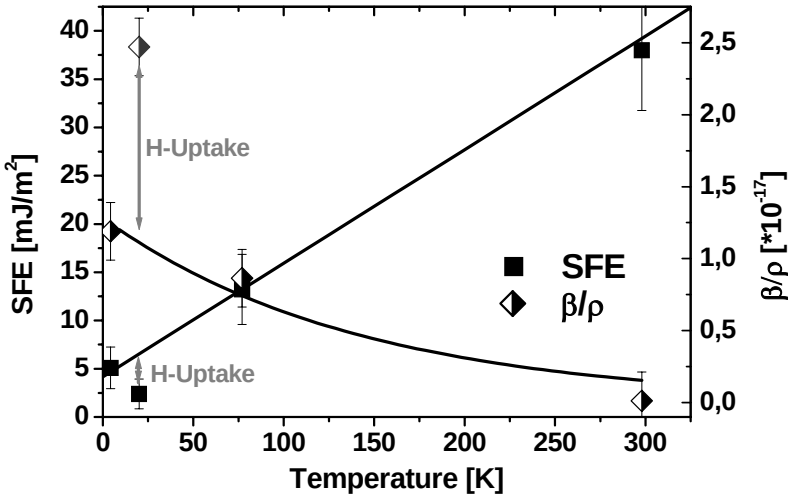

Fig.23: Influence of the temperature on the stacking fault energy and the deformation mechanisms in the steel 1.4439

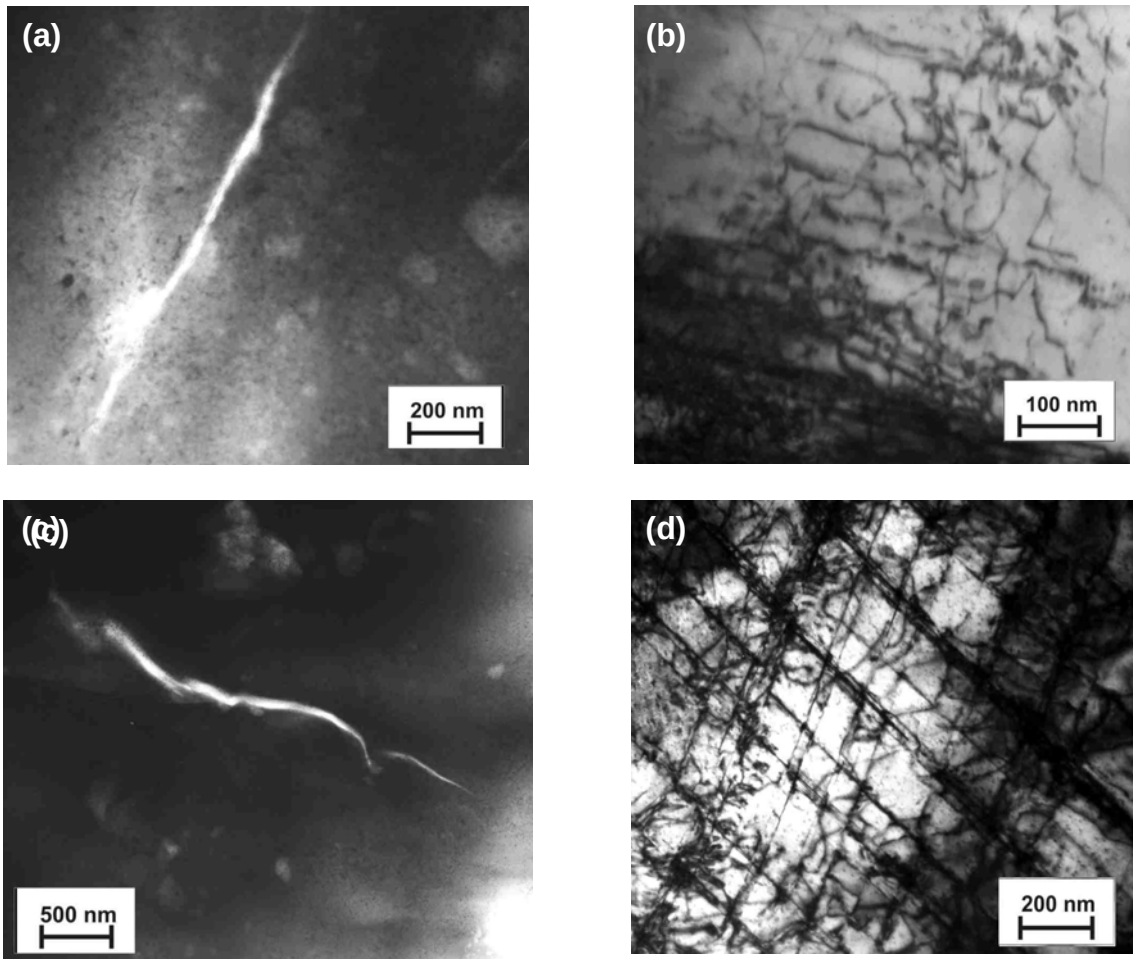

Fig.24: Crack initiation during friction in LH_2. (a) Microcrack in the alloy 1.4301, (b) Pile-up of planar arrays of dislocations at a twin boundary next to a crack in the steel 1.4301, (c) Microcrack in the alloy 1.4439, (d) Heavy slip band intersections next to cracked region in the alloy 1.4439

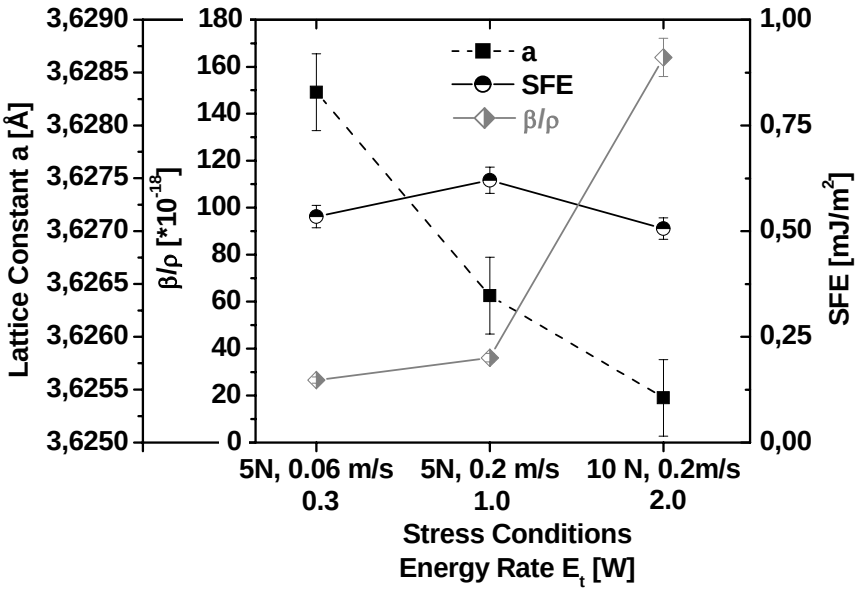

Fig.25: Influence of the stress conditions on the hydrogen uptake, stacking fault energy and deformation mechanisms in the steel 1.4452

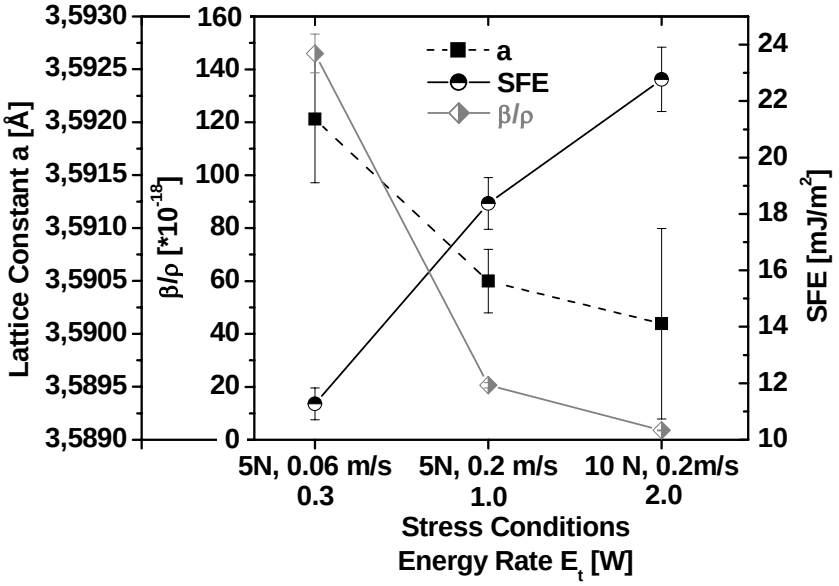

Fig.26: Influence of the stress conditions on the hydrogen uptake, stacking fault energy and deformation mechanisms in the steel 1.4876

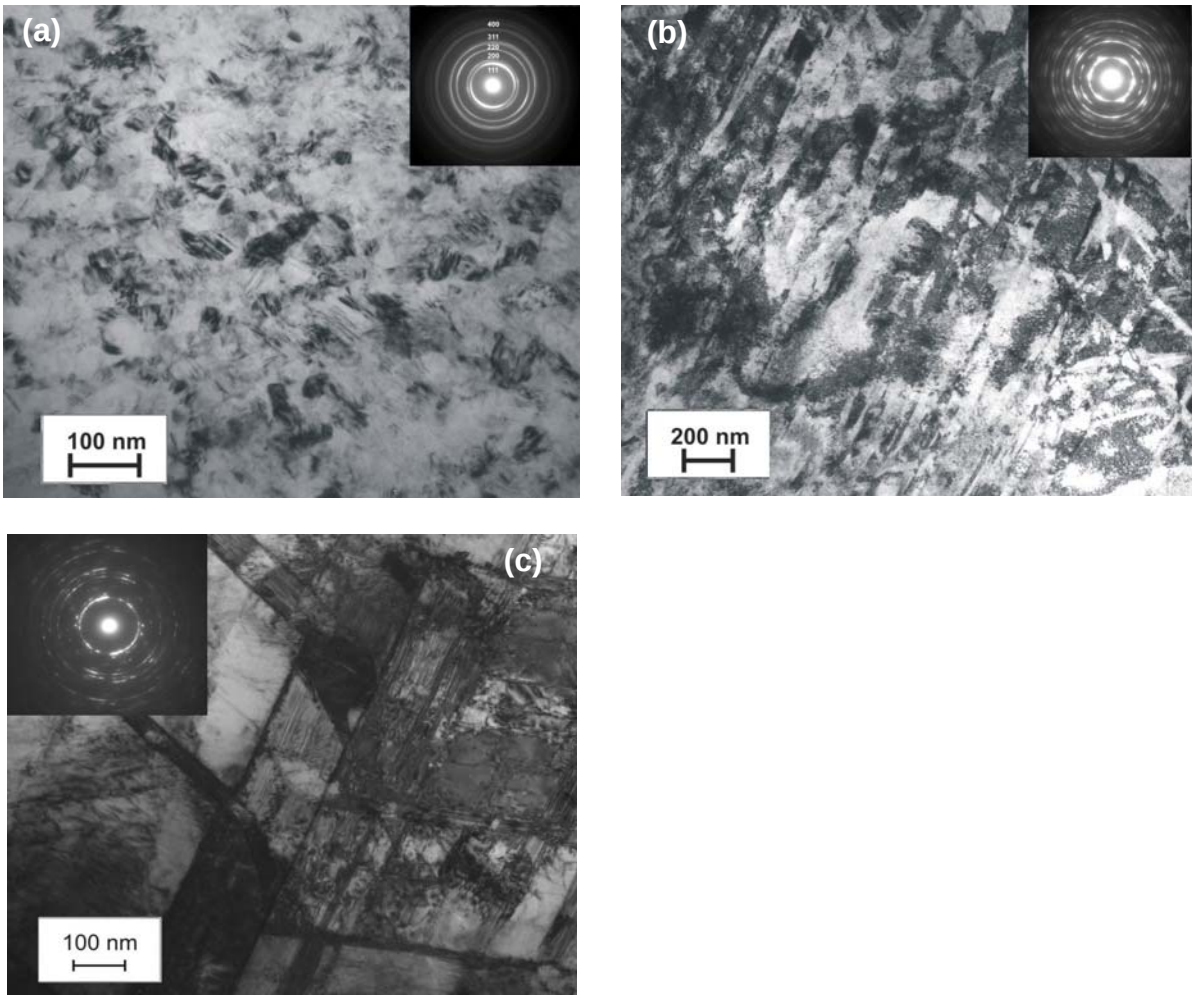

Fig.27: Nanocrystalline layers after friction: (a) 1.4439 at RT in air, (b) 1.4301 at 20K in LH_2, (c) heavily twinned zone in 1.4301 at 20K in LH_2

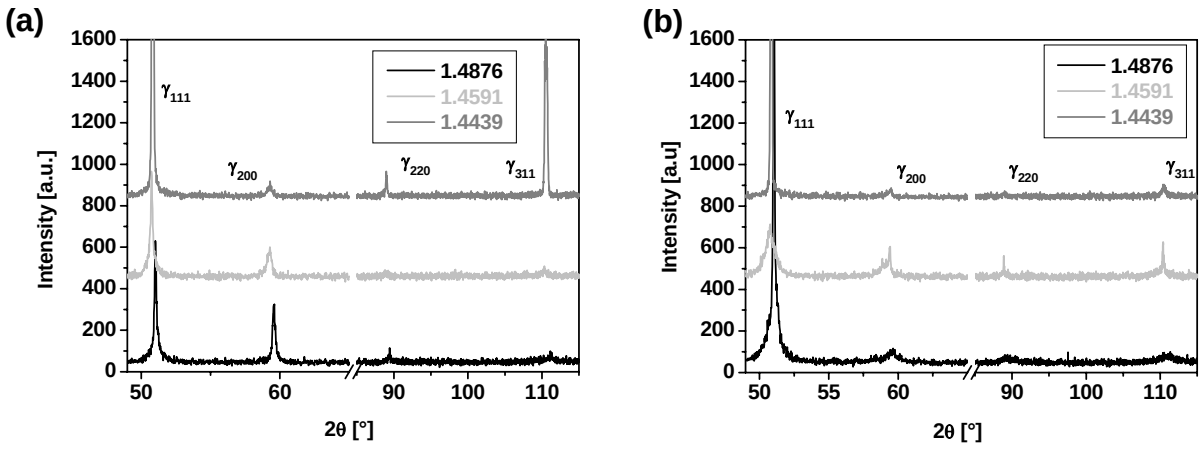

Fig.28: X-ray diffractograms from the wear scars produced in LH_2, 20 K with: (a) F_N = 5 N, v = 0.06 m/s; (b) F_N = 10 N, v = 0.2 m/s

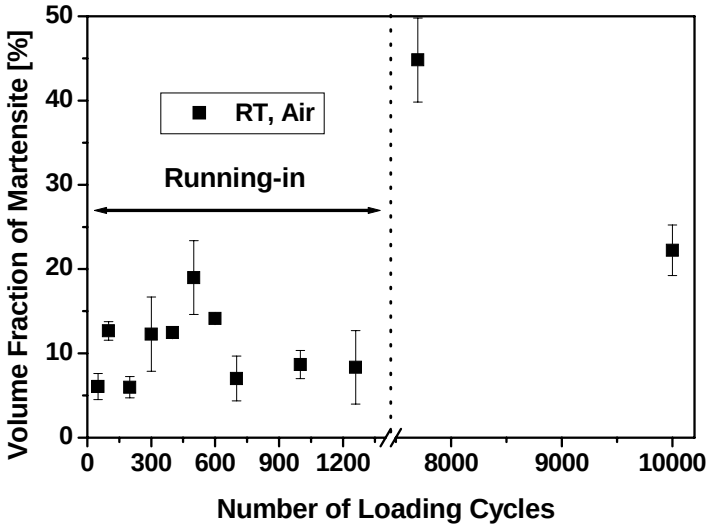

Fig.29: Evolution of the martensite content within the wear scar as a function of the loading cycles in the metastable alloy 1.4301

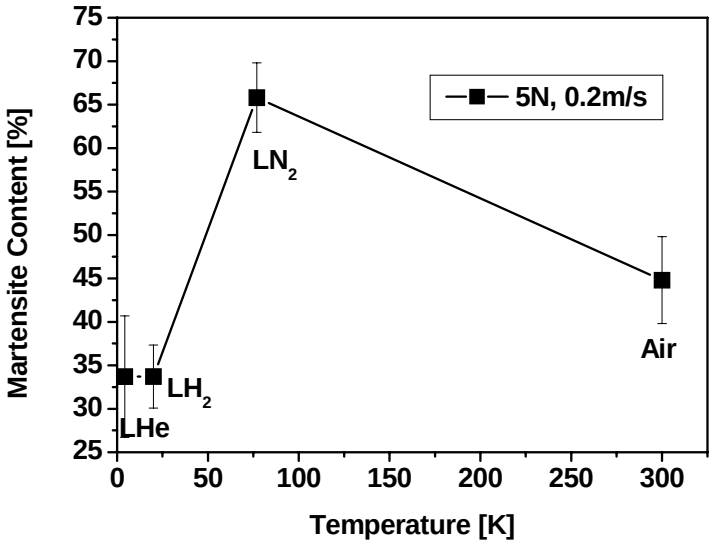

Fig.30: Influence of temperature on martensitic transformation in the metastable alloy 1.4301

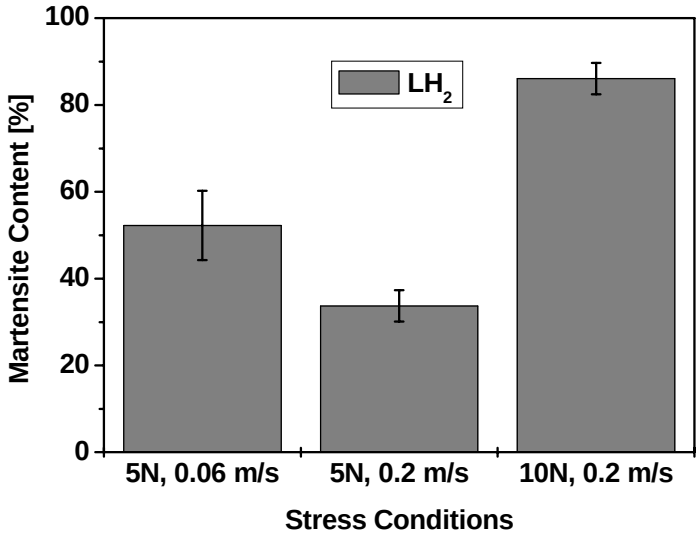

Fig.31: Effect of stress conditions on strain induced phase transformation in the steel 1.4301

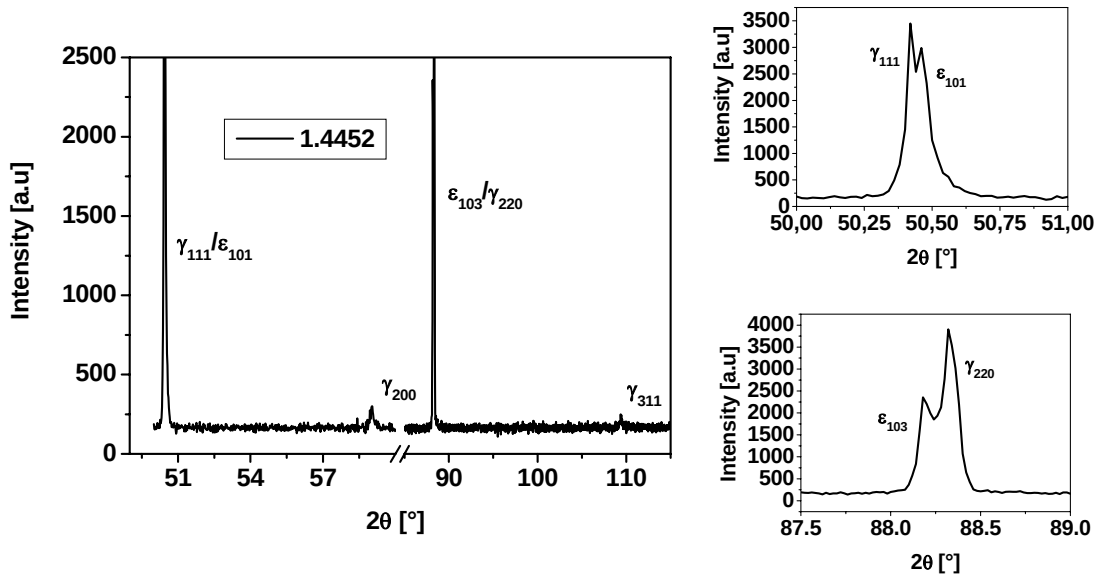

Fig.32: X-ray diffractogram from the wear scar of the steel 1.4452 showing the formation of ε-martensite after friction in LH_2 (F_N = 10 N, v = 0.2 m/s)

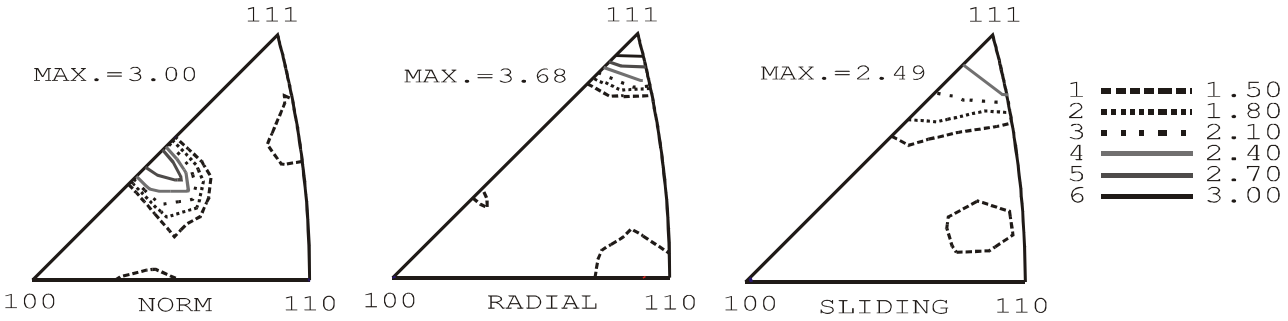

Fig.33: Texture formation in the austenite of steel 1.4301 after 1200 loading cycles at RT in air (F_N = 5 N, v = 0.06 m/s)

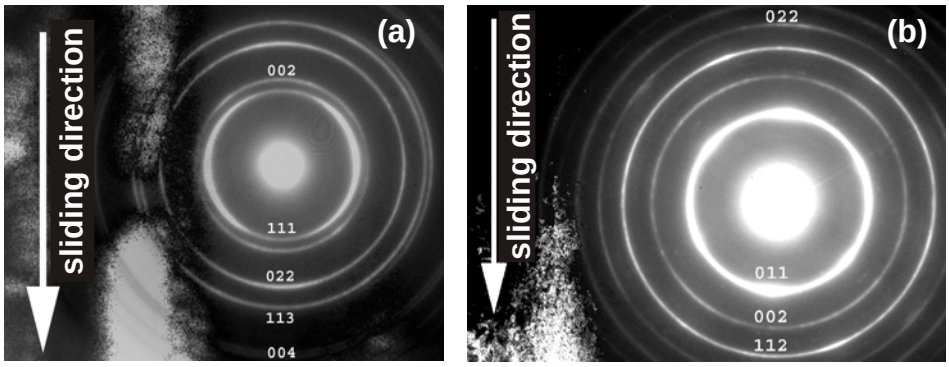

Fig.34: Texture formation within the nanocrystalline worn layer. (a) steel 1.4439 at RT in air, (b) steel 1.4301 at 20K in LH_2

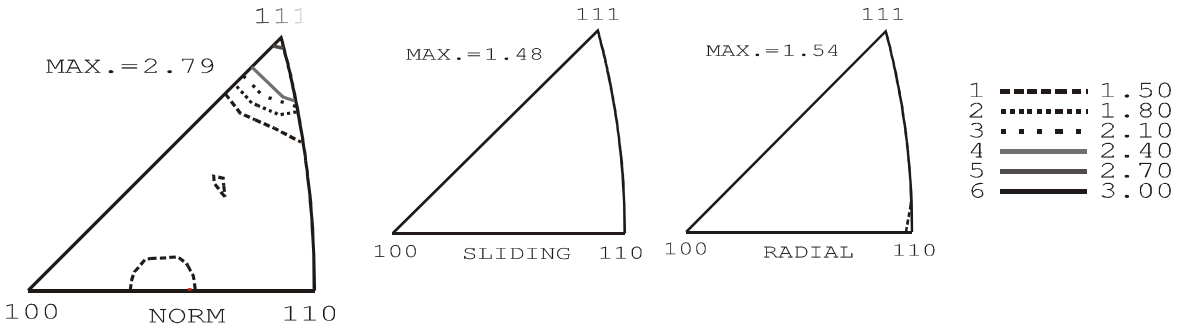

Fig.35: Texture formation in the austenite of steel 1.4301 after 7700 loading cycles at RT in air (F_N = 5 N, v = 0.06 m/s)

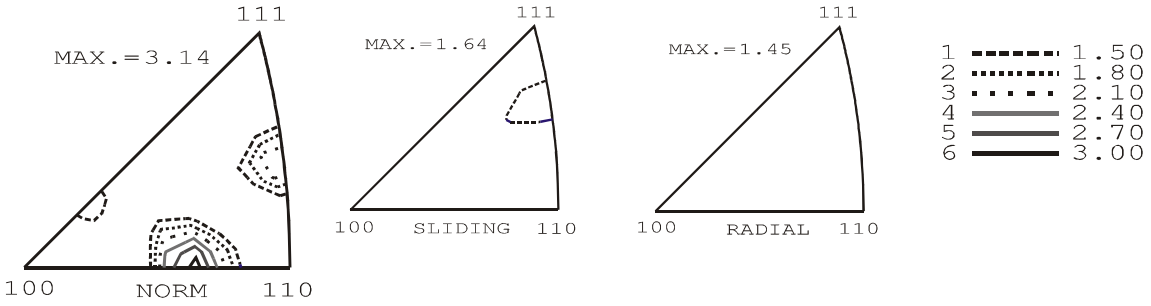

Fig.36: Texture formation in the martensite of steel 1.4301 after 1200 loading cycles at RT in air (F_N = 5 N, v = 0.06 m/s)

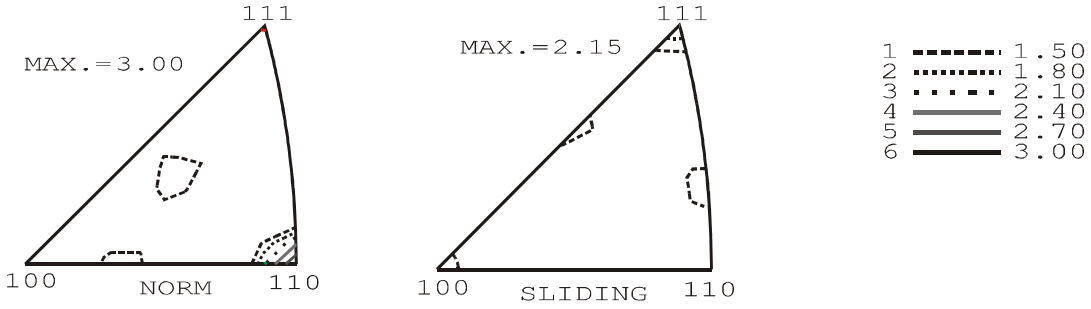

Fig.37: Texture formation in the austenite of steel 1.4439 after friction in LN_2 (F_N = 5 N, v = 0.06 m/s)

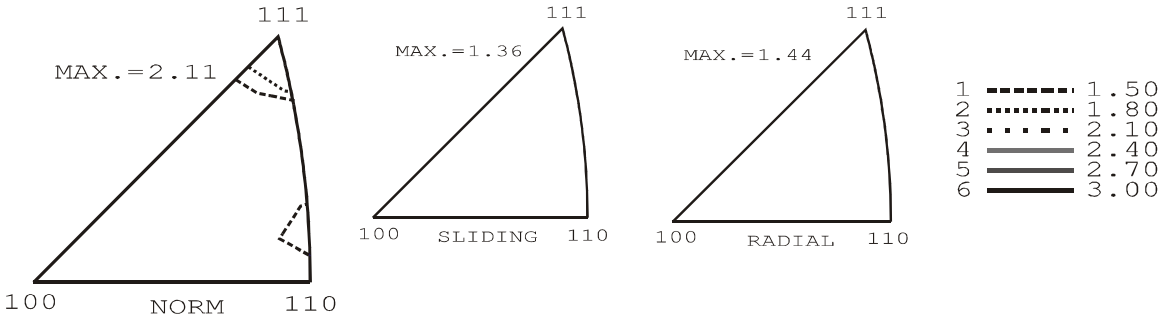

Fig.38: Texture formation in the martensite of steel 1.4301 after friction in LHe (F_N = 5 N, v = 0.06 m/s)

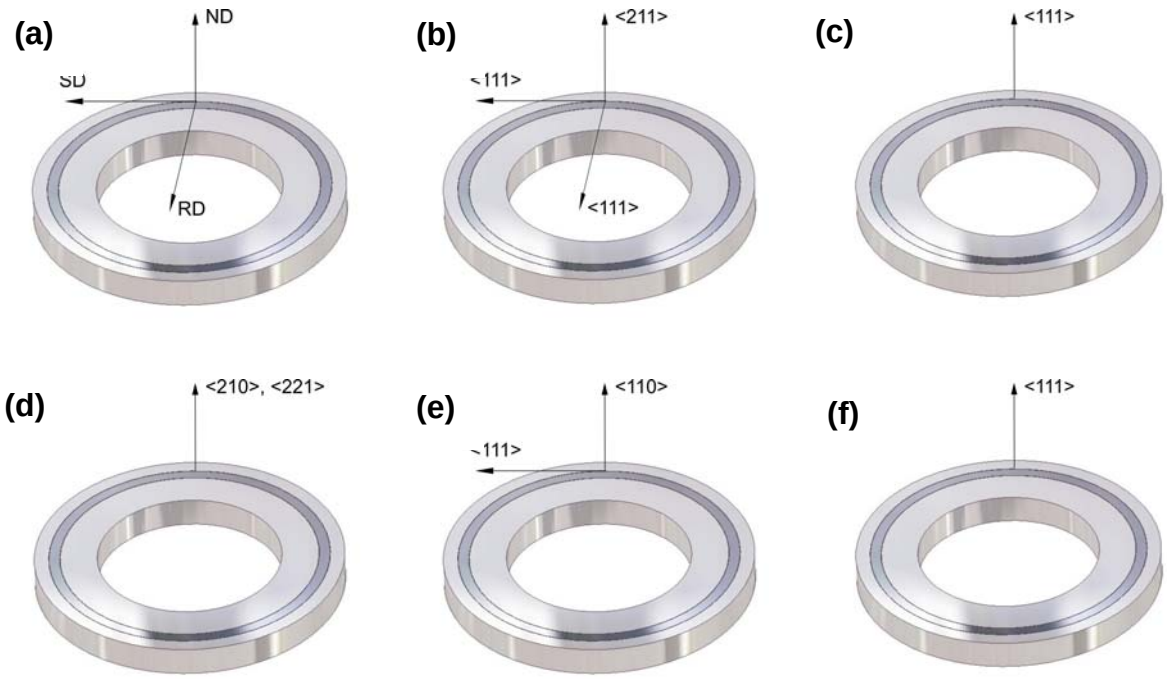

Fig.39: Texture formation in austenitic steels after wear: (a) definition of sample directions (ND = scar normal direction, SD = sliding direction, RD = radial direction), (b) first cycles at RT in austenite, (c) latter stages at RT in austenite, (d) martensite at RT, (e) austenite at low temperatures, (f) martensite at low temperatures

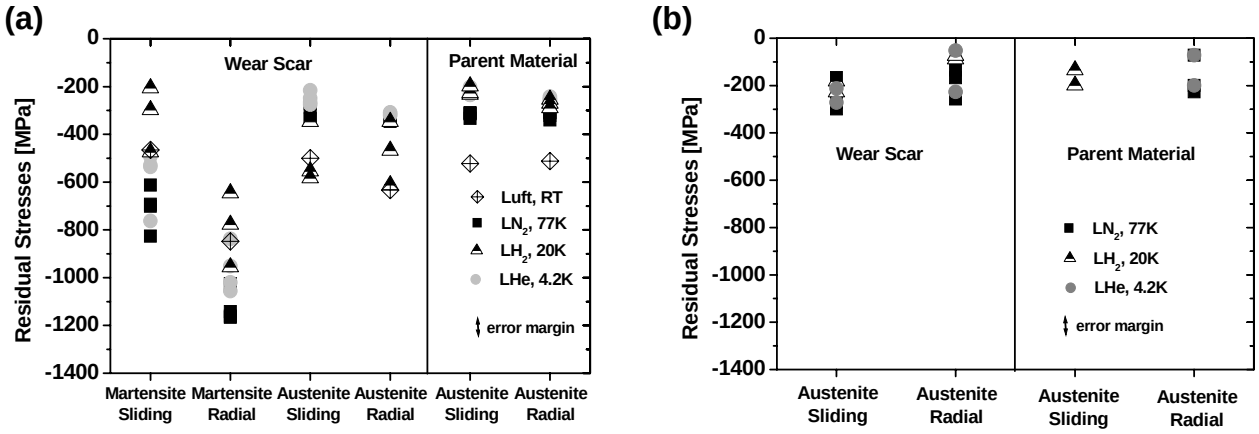

Fig.40: (a) Internal stress state in the steel 1.4301 after friction, (b) Internal stress state in the steel 1.4439 after friction

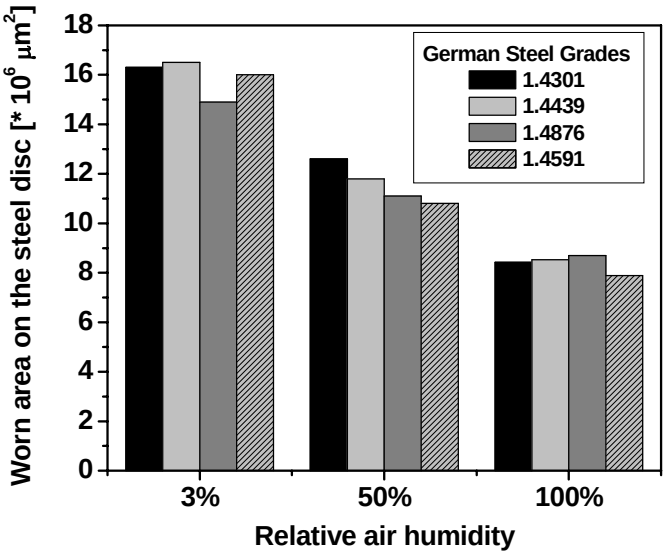

Fig.41: Effect of relative air humidity on the wear resistance at RT

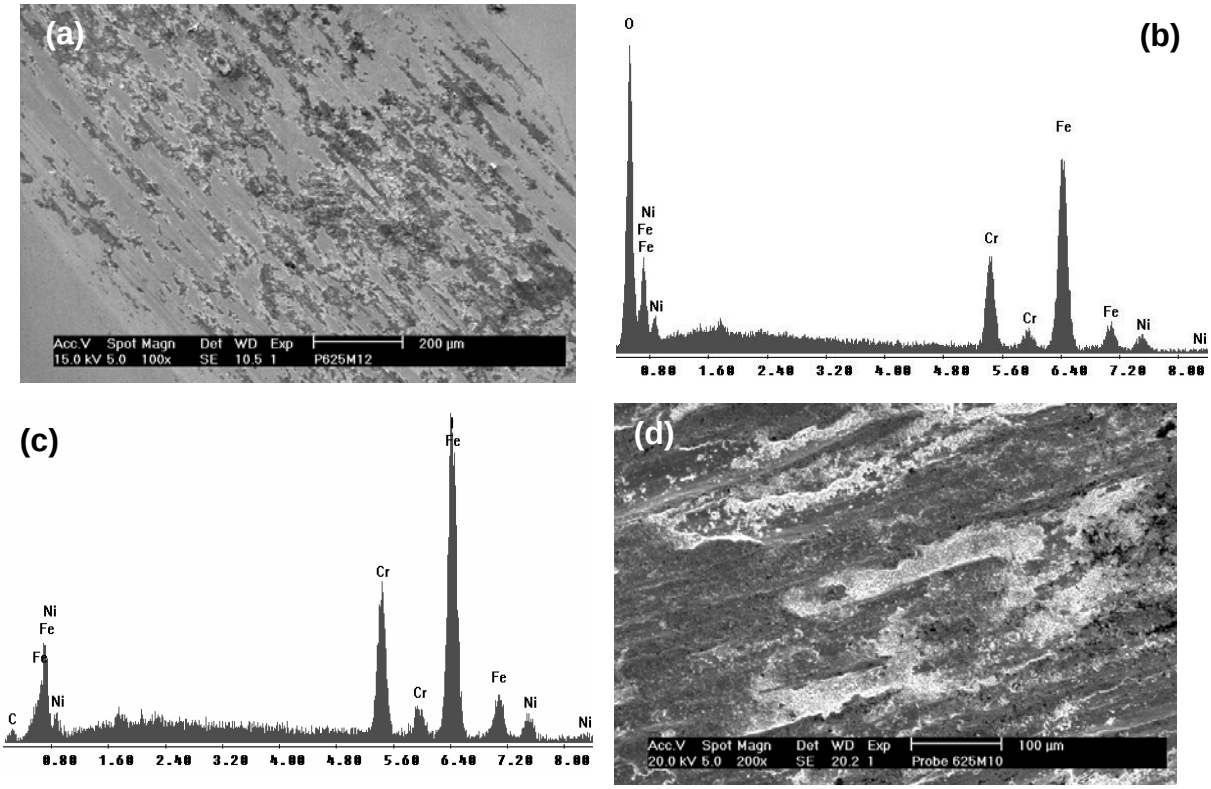

Fig.42: Wear scars in the steel 1.4301 (F_N = 5 N, Δx = 800 µm, f = 20 Hz) after oscillating friction in (a) 100% and (d) 3% relative air humidity, (b) EDX-analysis of the oxide layer formed and (c) of a wear scar zone, which was not covered by oxides, after friction in 100% relative air humidity

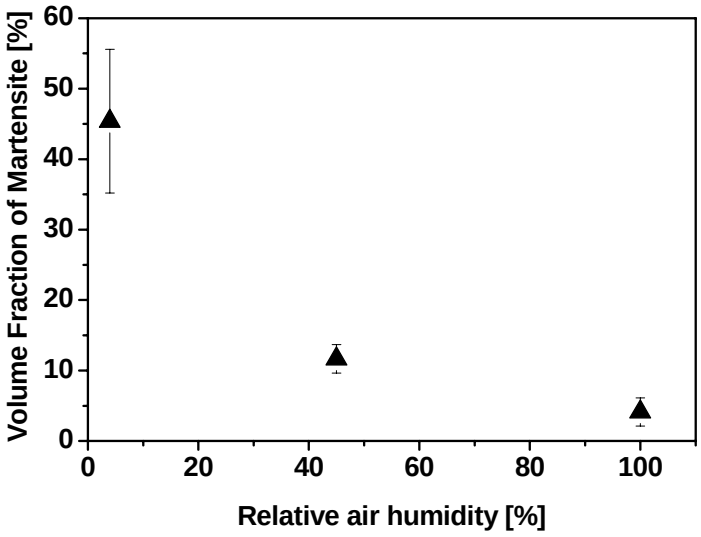

Fig.43: Effect of the relative air humidity on martensitic transformation in the alloy 1.4301

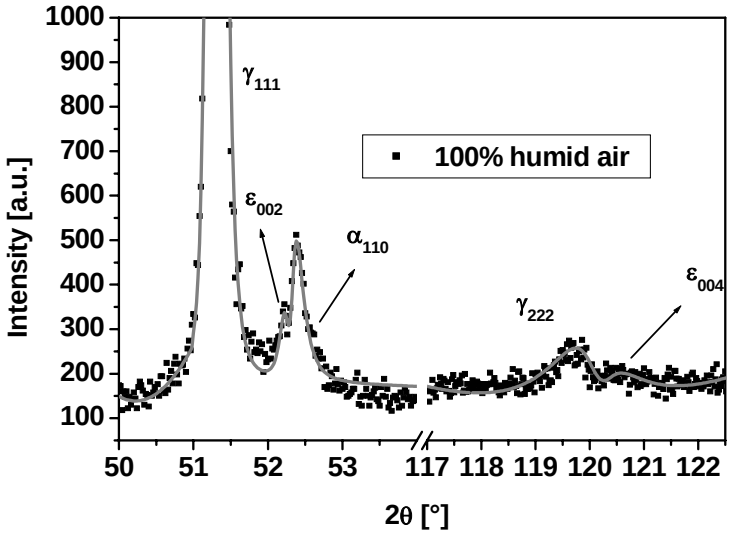

Fig.44: Presence of ε-martensite in the wear calotte after fretting of the steel 1.4301 in air with 100% humidity

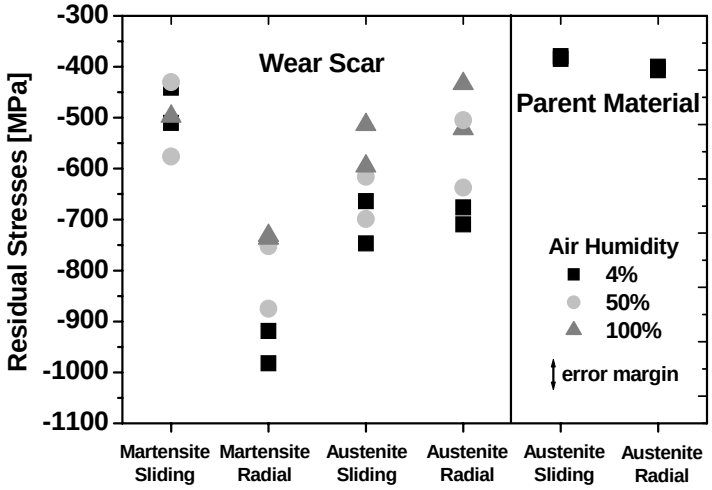

Fig.45: Internal stress state in the steel 1.4301 after oscillating friction at RT in different relative air humidities

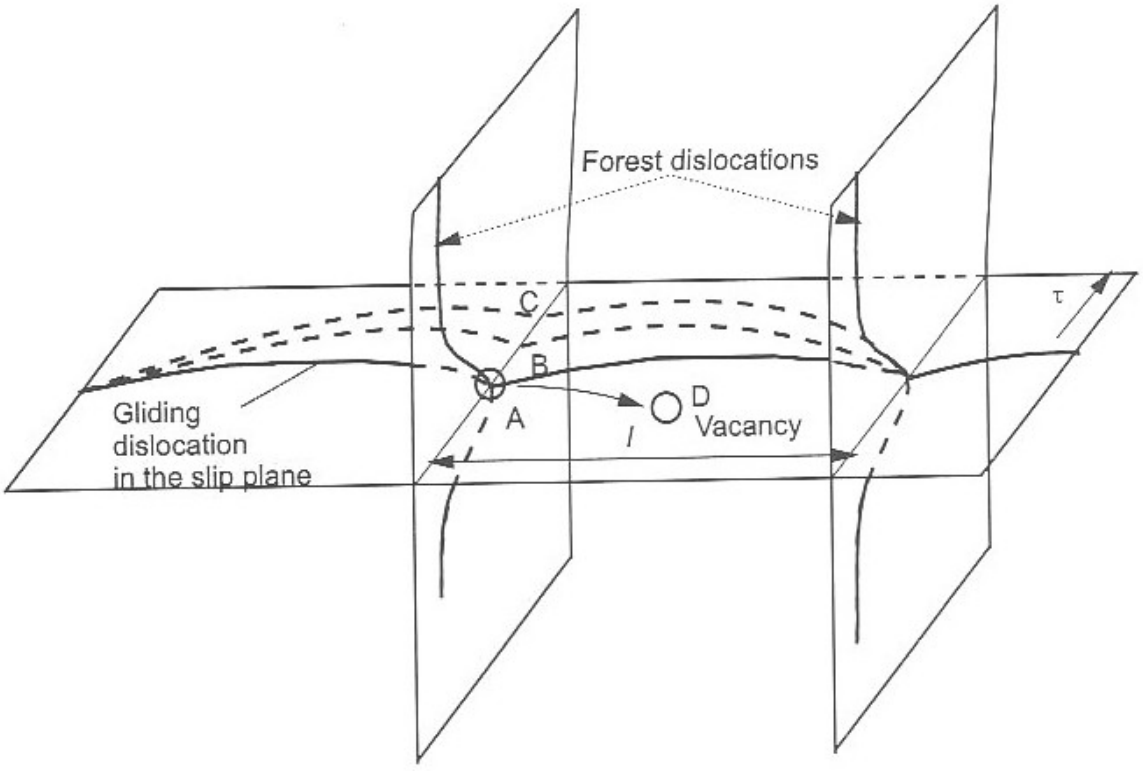

Fig.46: Interaction of gliding and forest dislocations producing a thermally activated generation of the vacancies [GAV99]

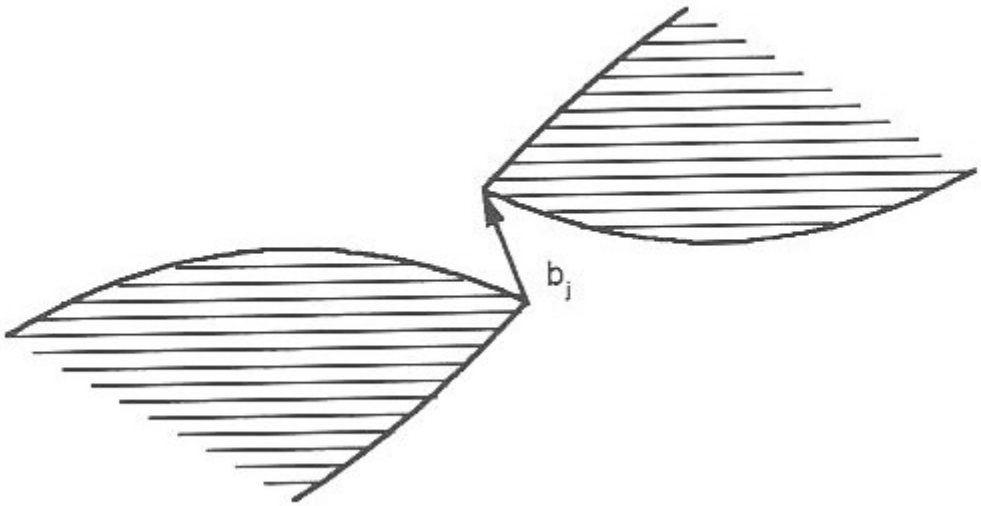

Fig.47: Constriction and formation of a jog during intersection of gliding extended dislocation with a dislocation forest [GAV99]

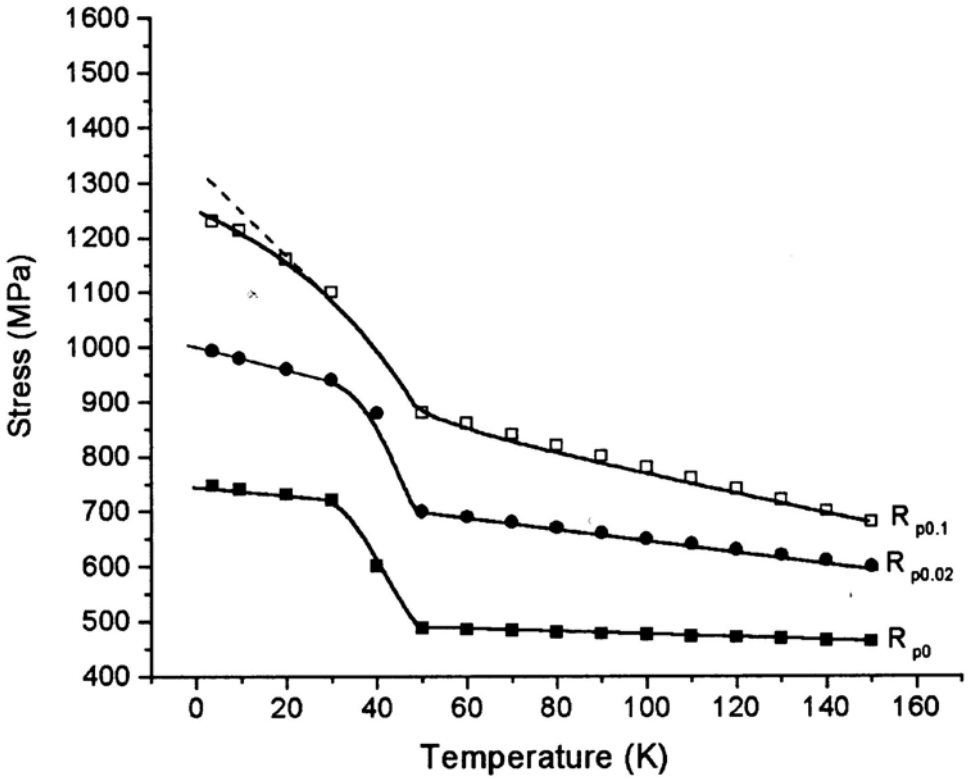

Fig.48: Effect of temperature on the tensile properties of the austenitic steel Cr25Ni15N0.35 [NYI93I]